Impact of faults on the remote stress state

Karsten Reiter[1], Oliver Heidbach[2,3], and Moritz. O. Ziegler[2]

[1]Institute of Applied Geosciences, TU Darmstadt, 64287 Darmstadt, Germany
[2]Helmholtz Zentrum Potsdam, Deutsches GeoForschungsZentrum GFZ, 14473 Potsdam, Germany
[3]Institute of Applied Geosciences, TU Berlin, 10587 Berlin, Germany

Correspondence: Karsten Reiter (reiter@geo.tu-darmstadt.de)

Abstract. The impact of faults on the contemporary stress field in the upper crust has been discussed in various studies. Data and models clearly show that there is an impact, but so far, a systematic study that quantifies the impact as a function of distance to the fault is missing. As there is a lack of dense data, we use here a series of generic 3-D-models to investigate which component of the 3-D-stress tensor is affected at what distance to the fault. Our focus is on the far-field beyond hundreds
5 of meters from the fault. The models test different approaches to implement faults, different material properties, different boundary conditions, variable orientation, and size of the fault. The results of our study show that beyond 1.000 m distance to the fault, the displacements along the fault and its strength contrast neither leaves an imprint on the orientation of the stress tensor nor in the magnitude of the principal stresses in the far field. This finding agrees with robust data from either stress magnitude measurements or areas where high-quality and high-resolution data on the change in orientation of the stress tensor
10 are available. The latter shows often continuous and gradual rotation of the stress tensor orientation over lateral spatial scales of 10 km or larger. These rotations cannot be attributed to faults as they only have an impact on scales < 1 km down to several meters only, as observed in numerous boreholes. Thus, we postulate that most stress orientation changes that are assigned to faults may have a different source.

15 ## 1 Introduction

The crustal stress field is a key driver of geodynamic processes such as the earthquake cycle (Brodsky et al., 2020; Hardebeck and Okada, 2018; Heidbach and Ben-Avraham, 2007; Wang et al., 2015) and is of great importance for the safe exploitation of georeservoirs and storage of energy or waste in the subsurface (Fuchs and Müller, 2001; Smart et al., 2014; Zoback, 2010). In this context the interaction between the stress field in the Earth's upper crust and pre-existing faults is a crucial issue (Blöcher
20 et al., 2018; Kruszewski et al., 2022; Li et al., 2023; Röckel et al., 2022; Schoenball and Davatzes, 2017; Yale, 2003).

For practical applications it is important, to understand and to quantify on which spatial scale the fault changes the stress state. Exemplified on the site selection process for a deep geological repository for high-level radioactive waste, the interest is to know the distance to a fault at which no significant changes of the stress components occur in order to build the repository

in a rock volume with homogeneous stress field conditions. In contrast to this, deep geothermal exploration targets faults or
25 fault networks since they provide higher permeability's compared to the rock matrix. Thus, the changes of the stresses in the
near-field of the fault and in its core or fracture network is of key interest to assess its dilation tendency (Ferrill et al., 2020;
Moeck and Backers, 2011; Seithel et al., 2019).

One of the key questions is, on what spatial scale faults change the stress field and to quantify which stress components
are affected. The only component of the 3-D stress tensor that is systematically compiled is the orientation of maximum
30 horizontal stress (S_{Hmax}, Heidbach et al., 2004, 2018). Areas with high data density revealed that the S_{Hmax} orientation can
rotate significantly on scales from 10's to 100's of kilometres (Heidbach et al., 2018, 2007; Lund Snee and Zoback, 2020;
Rajabi et al., 2017b; Tingay et al., 2006). The cause of this spatial variability has been investigated with generic geomechanical-
numerical and analytical modelling (e.g. Reiter, 2021; Sonder, 1990). These studies show that stiffness, strength and density
contrasts are certainly a key driver of spatial distributed changes of the S_{Hmax} orientation.
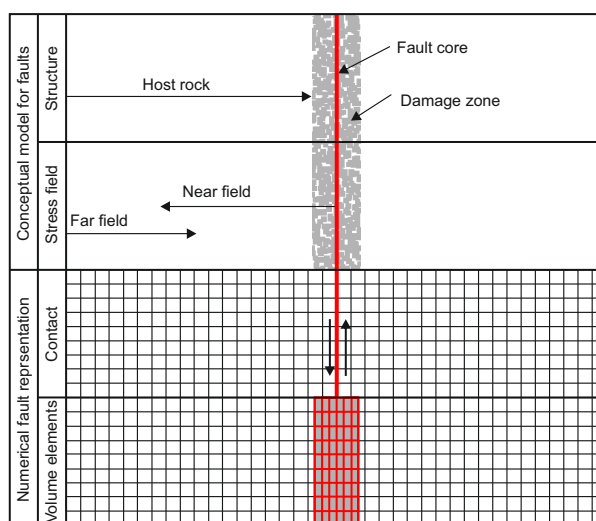
Figure 1. The general structure of a fault is described by the fault core, the damage zone, and the host rock (e.g., Caine et al., 1996; Faulkner
et al., 2003). The aim of the work is not to investigate the impact of a fault on the near field stress state. This would include the fault core,
the damage zone, and the neighbouring host rock. The focus of this study is on the far-field stress state, which is away from the fault of
about a few tens or hundred metres, to a maximum of a few kilometres. Numerical models usually use one or a combination of two principle
technical fault representations. Contact surfaces are a discontinuity within the mesh, where relative offset of the mesh is allowed, mainly
depending on the friction. The second method use a continuous mesh with elements having a lower stiffness or a failure criterion which
results in a distributed deformation within the defined fault representation elements.

35 Besides these findings, it was also hypothesised that active faults can cause rotations or magnitude variations as well (Dart
and Swolfs, 1992; Faulkner et al., 2006; Konstantinovskaia et al., 2012; Li et al., 2023; Schoenball et al., 2018; Yale, 2003).
This is confirmed on borehole scale since logging data show stress rotations on the meter scale by means of abrupt changes
in the orientation of borehole breakouts and drilling induced tensile fractures (e.g., Barton and Zoback, 1994; Rajabi et al.,

2017c). This was also observed in the scientific SAFOD borehole, drilled through the San Andreas fault (Zoback et al., 2011).

40 It clearly showed that there are indeed stress rotations on scales of one to several hundreds of meters occur, due to faults and that the amount of rotation changes with distance to the fault core (Hickman and Zoback, 2004). Significant variation of stress magnitudes in the vicinity of faults has been reported for China and Scandinavia (Li et al., 2023; Stephansson and Ångman, 1986), but from these studies it is not clear which stress tensor component is affected as a function of distance to the fault. Furthermore, the mix of different methods that are used to estimate stress parameter from very shallow locations near surface

45 as well as the lack of a rigorous uncertainty assessment makes it difficult to assess whether the observed changes are significant and if they can be exclusively attributed to the nearby fault.
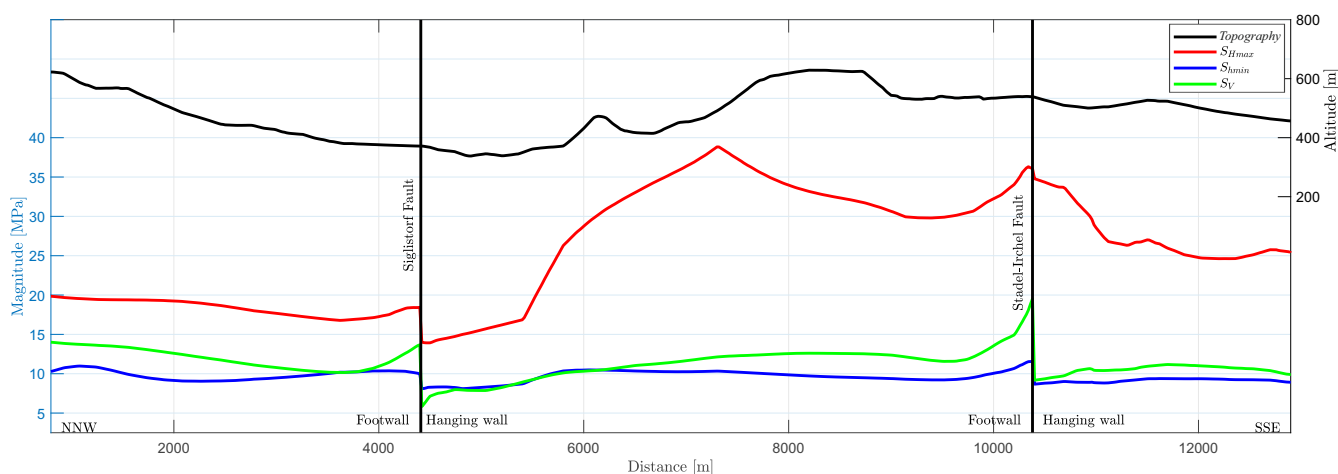
Figure 2. Plot of stress components along a NNW-SSE profile at approximately 400 m true vertical depth within the Nördlich Lägern model (Hergert et al., 2015). The largest and smallest horizontal principal stress (S_{Hmax} and S_{hmin}), the vertical stress (S_V) and the von Mises stress are shown. Additional shown is the topography from the model. The location of the implemented Siglistdorf- and Stadel-Irchel fault are indicated by black vertical lines. Stress magnitudes changes are significant next to the fault, but they are even more variable due to variable topography, rock stiffness or other factors.

The only method to test that are generic models, using geomechanical numerical methods. There are several technical methods available to mimic faults or fault zones numerically; for method overview see Henk (2020). Where using the continuum method, a fault is represented by selected elements with different behaviour, e.g., a lower Young's modulus (e.g., Cappa

50 and Rutqvist, 2011), a plastic behaviour (e.g., Mohr-Cloulomb) or viscous behaviour. In contrast to that, using the discontinue method, the fault is represented by contact elements (e.g., Buchmann and Connolly, 2007; Hergert et al., 2015) which allow offset along these structures (Fig. 1, Tab. 1). The Finite Element Method (FEM) is often used for such studies. Another discontinue method, where the geometry is divided into several individual elements (circles or spheres, etc.) is the Discrete Element Method (DEM, e.g., Cundall and Hart, 1992; Yoon et al., 2014), which will not be used here.

55 The impact of faults has also been investigated by several authors using forward models. These studies (e.g. Tab. 1) either focus on how to technically implement faults into geomechanical-numerical models (Prévost and Sukumar, 2016; Treffeisen

Table 1. List of some example studies, using either a continuous or discontinuous mesh as fault representation (Fig. 1). Discontinuities are represented by contact elements or comparable methods (Contact). Another way to represent faults is a continuous mesh having a somehow weaker material definition (elastic, plastic or viscous). These are 2-D elements within a 2-D Mesh or 3-D Elements in a 3-D mesh (Volume). Many models apply the Finite Element Method (FEM), others use the Finite Difference Method (FDM), Finite Volume Method (FVM), the Discrete Element Method (DEM). (The list does not claim to be complete.)

	Authors	Contact	Volume
Finite Element Method	Tommasi et al. (1995)	-	x
	Buchmann and Connolly (2007)	x	-
	Xing et al. (2007)	x	-
	Hergert et al. (2011)	x	-
	Reiter and Heidbach (2014)	x	-
	Pereira et al. (2014)	-	x
	Hergert et al. (2015)	x	-
	Franceschini et al. (2016)	x	-
	Zhang et al. (2016)	-	x
	Meier et al. (2017)	-	x
	Schuite et al. (2017)	-	x
	Treffeisen and Henk (2020b)	x	x
	Reiter (2021)	x	-
other methods	Homberg et al. (1997)	x	-
	Sánchez D. et al. (1999)	x	-
	McLellan et al. (2004)	-	x
	Camac and Hunt (2009)	x	-
	Cappa (2009)	-	x
	Cappa and Rutqvist (2011)	x	-

and Henk, 2020b) or on specific geological settings (Chéry et al., 2004; Fitzenz and Miller, 2001; Hergert and Heidbach, 2011; Meier et al., 2017; Yoon et al., 2017). As an example, Fig. 2 plots stress components along a horizontal line at approximately 400 m true vertical depth within a model from northern Switzerland (Hergert et al., 2015). However, resulting stress changes

60 are affected by other factors too, such as topography or variable material properties etc.

Previous studies show that faults have certainly an impact, but a systematic approach is still missing. They do not provide a quantification, which component of the stress tensor is affected by the stress changes near the fault. In this paper we investigate systematically the change of individual stress tensor components with distance to the fault. In particular we determine the changes of the magnitudes of the maximum and minimum horizontal stress (S_{Hmax} and S_{hmin}), respectively, the vertical stress

65 (S_V) and the von Mises stress as well as the orientation of the stress tensor by means of the S_{Hmax} azimuth in different settings regarding fault and rock properties, stress regime and fault structure. Again, our focus is the far-field perspective, i.e.

at distances beyond 100 m from the fault core (Fig. 1). Thus, this work does not aim to answer the question to what extend the stress tensor components are affected in the near field.

2 Model set-up

2.1 Model concept

70

We set up generic 3-D models with model dimensions, rock properties and an initial stress state that are like the one from a 3-D geomechanical-numerical model of a potential siting area for a high-level radioactive waste disposal site in Northern Switzerland, presented by Hergert et al. (2015). For implementation in the model, faults are represented by contact elements, which allow an offset, or 3-D elements which are elastically or plastically weaker than the surrounding rocks (Fig. 1).

2.2 Partial differential equation and solution scheme

75

The two key components of a static stress state are a result from volume forces due to gravity and surface forces from plate tectonics. Neglecting acceleration, the resulting partial differential equation is the equilibrium of forces. For the upper crust assuming linear isotropic elasticity is a good approximation to describe the stress-strain relation (e.g., Tesauro et al., 2012). Thus, for simplicity the three key model parameters in our study are density, the Young's modulus (E) and the Poisson's ratio (ν). Additionally, the Mohr-Coulomb criteria, using the friction (μ) and the cohesion (C), will be used for some models. As we introduce a fault in our model with different techniques, we solve the problem numerically using the FEM.

80

2.3 Geometry and material properties

The reference model has an extent of 10 km in each horizontal and 3 km in vertical direction (Fig. 3). The model is intersected in its entirety in the centre by a 60° inclined fault, represented by cohesionless contact elements with a friction coefficient of $\mu = 0.4$ (friction angle $\phi = 21.8°$). The main shortening direction is perpendicular to the strike of the fault.

85

Homogeneous linear elastic and isotropic material properties are assigned to the reference model, having a Young's modulus of $E = 15$ GPa, a Poisson's ratio of $\nu = 0.27$ and a density of $\rho = 2550$ kg m^{-3}. The FE-mesh for the reference model has a resolution of 50 m in the X- and Z-direction, and 500 m in the Y-direction. The mesh was created with HyperMesh 2017 and 2019 respectively; the used solver is Abaqus 6.14.1.

2.4 Model scenarios

90

The scope of the study is on various factors, which probably contribute to different effects on the stress state in the broader vicinity of faults. These include the element resolution (pre-tests), the representation of the fault by contact elements with a variable friction coefficient, representation of the fault by elastic weaker elements, or by elements with elasto-plastic rheology, the inclination of the fault, the strike direction relative to the shortening direction, the variation of the rock stiffness (Young's
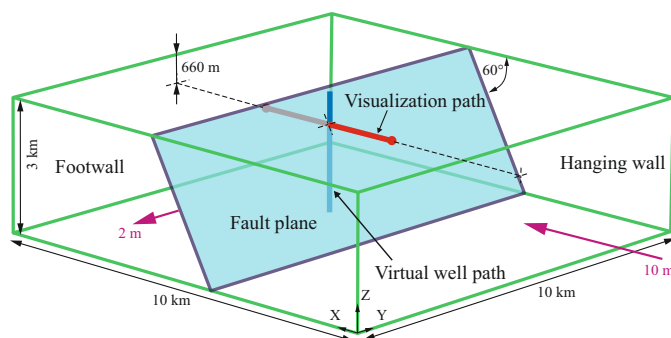
Figure 3. The model extend ($10 \times 10 \times 3 \, \text{km}^3$, in green) with the fault (blue plane), inclined by $60°$ (dip angle), in red the visualisation path at a depth of $660 \, \text{m}$ along which the stress magnitudes are shown. The blue vertical line indicates the location of a vertical well (Fig. 4). The displacement boundary conditions in purple are $10 \, \text{m}$ shortening ($\epsilon = -1 * 10^{-3}$) in X-direction (perpendicular to the strike direction of the fault), which then governs the S_{Hmax} magnitude, and $2 \, \text{m}$ of dilation ($\epsilon = 2 * 10^{-4}$) in Y-direction (parallel to the strike direction of the fault), which then drives the S_{hmin} magnitude.

95   modulus) and the size of the fault and model itself. In order to allow a good readability of the study, specific variations of the model are always briefly explained before presenting the modelling results.

2.5   Initial stress state and boundary conditions

We implement an initial stress state of the model that is in equilibrium with the gravitational forces without resulting in any significant displacement along the fault and the model geometry. We follow the technical procedure as explained in Hergert

100   et al. (2015). In a second step we apply along the model lateral boundaries displacement boundary conditions that result in tectonic stresses throughout the model volume. The main shortening of the reference model is perpendicular to the fault (X-direction) in the order of -10 m ($\epsilon = 1 * 10^{-3}$), which then corresponds to the S_{Hmax} orientation. Parallel to the fault strike (Y-direction), the model undergoes a slight dilation of $2 \, \text{m}$ ($\epsilon = 2 * 10^{-4}$), which is then the orientation of S_{hmin} (Fig. 3). The stress magnitudes resulting from the boundary conditions are shown in Fig. 4 along a vertical synthetic well path in the centre of

105   the model. This stress state is in general agreement with stress magnitude data that were derived from a measurement campaign in Northern Switzerland using >150 Mini-Hydraulic Fracturing and Sleeve Re-Opening test (Desroches et al., 2021).

2.6   Stress definition and visualisation

The 3-D stress state of the Earth's crust is described with a second rank tensor ($\boldsymbol{\sigma}$, Jaeger et al., 2011) with nine components, but due to its symmetry only six components are independent from each other. The stress state can also be described with the

110   magnitudes and orientations of the three principal stresses. These principal stresses are named from the largest to the smallest as $\sigma_1 > \sigma_2 > \sigma_3$. As common in geoscience, compressive stress magnitudes are positive and tensile stress is negative.
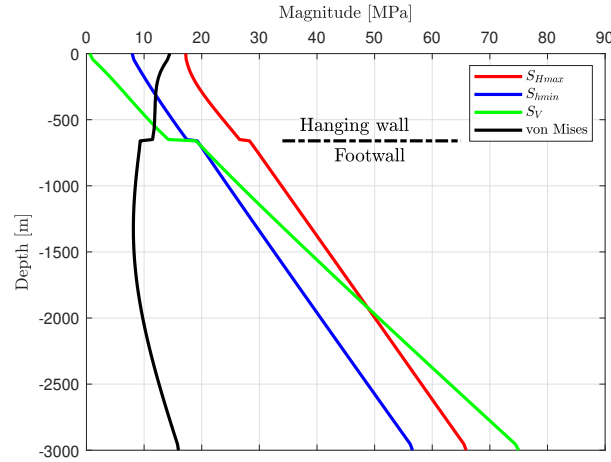
Figure 4. Virtual vertical well path in the centre of the reference model. Shown are the resulting stress components, which are S_{Hmax}, S_{hmin}, S_V and the von Mises stress. The fault with a friction coefficient of $\mu = 0.4$ is traversed at a depth of -660 m. It is visible that when crossing the fault from the hanging wall to the footwall block, there is a sudden increase of S_{Hmax} and S_V, but S_{hmin} is only little effected.

Here, we use the differential stress (σ_D) and it's 3-D-equivalent, the von Mises stress (σ_{vM}; Mises, 1913) to visualise the stress state (Eqs. 1 and 2).

$$\sigma_D = \sigma_1 - \sigma_3 \tag{1}$$

$$\sigma_{vM} = \sqrt{\frac{1}{2}(\sigma_1 - \sigma_2)^2 + (\sigma_2 - \sigma_3)^2 + (\sigma_3 - \sigma_1)^2} \tag{2}$$

115

Furthermore, it is assumed that the vertical stress (S_V) is a principal stress (Eq. 3). The two other principal stresses are in the horizontal plane and are labelled as the minimum and maximum horizontal stresses (S_{hmin} and S_{Hmax}).

$$\boldsymbol{S}_V = \int_0^z \rho g z, \tag{3}$$

The relative ratio of these three principal stresses defines the stress regime (Anderson, 1905, 1951):

Normal faulting stress regime	NF	$S_V > S_{\text{Hmax}} > S_{\text{hmin}}$
Strike slip stress regime	SS	$S_{\text{Hmax}} > S_V > S_{\text{hmin}}$
Thrust faulting stress regime	TF	$S_{\text{Hmax}} > S_{\text{hmin}} > S_V$

120   The model results are presented here in the same way whenever possible. Both the reduced stress tensor and the von Mises stress are used to visualise the influence of a fault on the stress state. The results of the models are plotted along a horizontal path at a depth of -660 m (Figs. 3 and 5) for the reference model. This path is always parallel to the main shortening direction (X) and extends from the footwall block at -3.000 m through the fault at 0 m to +3.000 m in the hanging wall block.
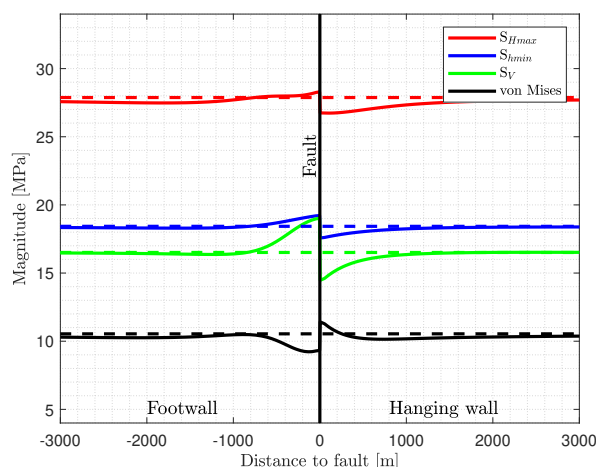
Figure 5. Stress magnitude visualisation of the reference model from -3.000 m (footwall - left) to $+3.000$ m (hanging wall - right) for a constant depth of -660 m. Used are linear elastic material properties and a friction coefficient of $\mu = 0.4$ for the fault at 0 m, represented by the black vertical line. The dashed lines represent in comparison results of an similar model without a fault.

2.7   Pre-test: Mesh resolution

125   The impact of the mesh resolution and sufficiency was investigated by varying the mesh size, using elastic material properties only, like the reference model. An all-sided resolution of 1.000, 500, 250 and 100 m is tested; a finer resolution has been used with an element size of 50 m in the main shortening and depth direction (X and Z), for which the resolution parallel to the fault (Y) is 500 m.

128   The model with the coarsest resolution (1.000 m) provides stress magnitudes that deviate significantly from the other models
130   (red line in Fig. 6). Even for the model with a resolution of 500 m (magenta line in Fig. 6), the deviation from the higher-resolution models, at a distance greater than 1.000 m is clearly visible. All finer-resolution models (≤ 250 m), have only small differences close to the fault (< 1.000 m; Fig. 6). This shows, that all models with a resolution of 250 m and finer have a sufficient mesh resolution. A finer mesh is only useful if the magnitude close to the fault is of interest, which is not the case in this study.
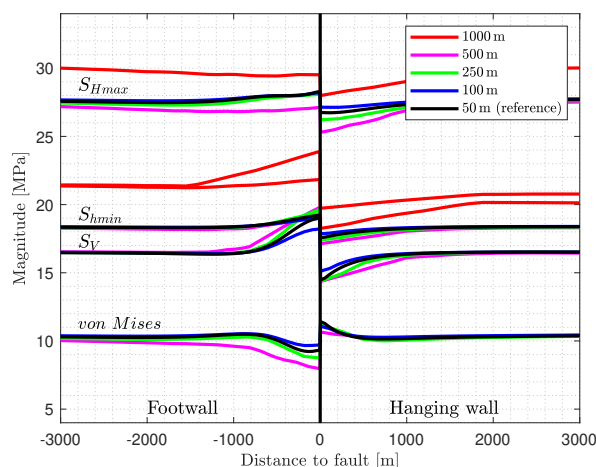
Figure 6. The impact of the mesh resolution is compared. The coefficient of friction of the fault is $\mu = 0.4$ for all models. The coarse resolution models, with $1.000\,\mathrm{m}$ (red) as well as $500\,\mathrm{m}$ (magenta) show significant deviations from the reference model with a resolution of $50\,\mathrm{m}$ (black), while the models with a resolution of $100\,\mathrm{m}$ and $250\,\mathrm{m}$ (green and blue) show only slight deviations close to the fault.

3   Results

3.1   Reference model

Within the reference model, the fault is represented by a contact surface ($\mu = 0.4$, $C = 0$). As a result, the components of the reduced stress tensor increase in the footwall close to the fault and decrease in the hanging wall (Fig. 5). S_V and S_hmin rise to a similar level ($+3\,\mathrm{MPa}$ and $+1\,\mathrm{MPa}$) within the footwall block near the fault. An opposite behaviour is observed for the von Mises stress. S_Hmax, however, increases only slightly close to the fault ($<1\,\mathrm{MPa}$); which is the reason for the decrease of the von Mises stress near the fault. Corresponding to that changes the stress magnitudes decrease next to the fault within the hanging wall block, the largest amount is for S_V, resulting in a slight increase of the von Mises stress. Significant stress changes of more than $1\,\mathrm{MPa}$ occur within less than $1.000\,\mathrm{m}$ away from the fault.

3.2   Friction coefficient

In geomechanics and seismology faults are usually parameterised using the friction coefficient and the cohesion. Commonly, a friction coefficient between 0.6 and 0.85 is assumed (Byerlee, 1978) but examples exist of significantly smaller friction coefficients (Di Toro et al., 2011). However, to investigate the influence of the frictional properties of a fault based on the reference model, the friction coefficient is varied from very low ($\mu = 0.1$) to very large ($\mu > 1$). Due to technical limitations cohesion will be always zero.
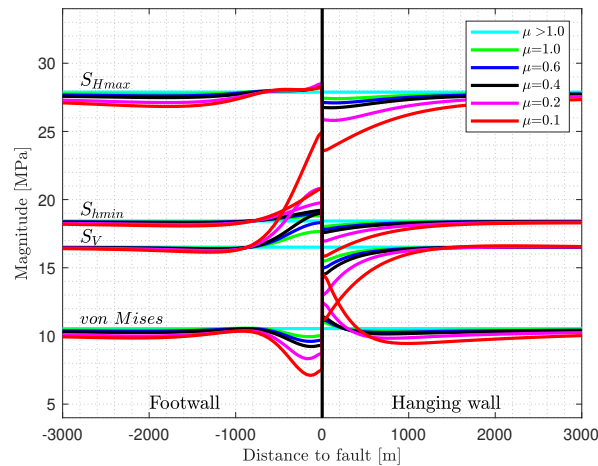
Figure 7. Impact of a variable friction coefficient on the stress state. Plotted are the S_{Hmax}, S_{hmin} and S_V as well as the von Mises stress. The graph with the friction angle of $\mu = 0.4$ is the reference model (Fig. 5).

150   Using a very large friction coefficient ($\mu > 1$), there is no visible influence by the fault on the stress magnitudes (Fig. 7), the stress magnitudes are identical to a continuous mesh without a contact surface (dashed line in Fig. 5). In contrast, for a low friction case ($\mu = 0.1$), stress variation is significant near the fault. The general pattern is similar as for the reference model, but the increase (footwall: +8 MPa) and decrease (hanging wall: -5 MPa) of S_V is much larger. Similar, but not that large stress changes are to observe for S_{hmin}, +2 MPa for the footwall und -2 MPa for the hanging wall block. The drop of S_{Hmax} in the

155 hanging wall block is significant (-4 MPa), whereas the increase in the footwall block next to the fault is negligible. However, a S_{Hmax} decrease of about -1 MPa is visible in both, the footwall- and hanging wall block, even between 1.000 to 3.000 m away from the fault. Variation of the von Mises stress is mainly driven by the variation of S_V. It is mostly σ_3, trimmed by the fact, that S_V becomes significant larger then S_{hmin} in the footwall block about 500 m away from the fault for the models with low friction contact definition.

160   Overall comparison of the models with a different friction in Fig. 7 show, that the stress perturbations gradually decreas with an increase of the friction coefficient. A stress variation of > 1 MPa is limited to a distance of ≈ 1 km, except for S_{Hmax} in the hanging wall block. None of the variation result in a visible change of the S_{Hmax} orientation, it is always parallel to the maximum displacement (X-direction).

3.3   3-D-fault representation by elastic weak elements

165 The representation of a fault by a 2-D plane is not realistic for the immediate vicinity of the fault where a zone of damaged rock is expected. A more realistic approach seems to be the representation by a 10 m thick layer of elements with elasto-plastic rheology (Fig. 8 a). This simulates the reduced stiffness due to the damage zone in and around the fault core (e.g., Faulkner
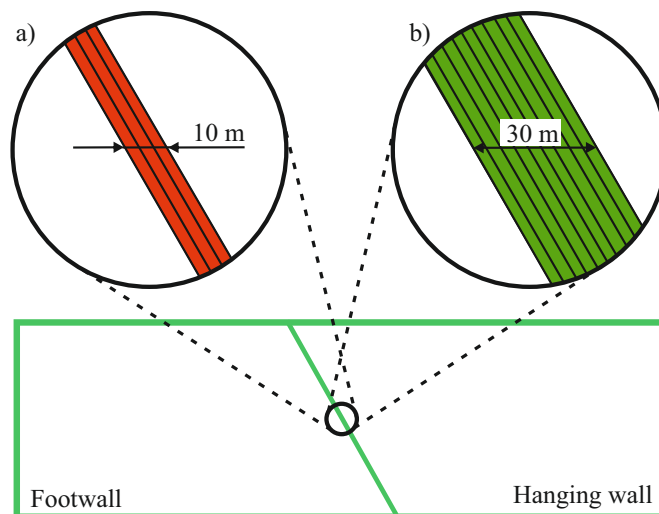
Figure 8. Sketch visualising the representation of the fault by elastically weak 3-D-elements with a thickness of a) 10 m made from three elements or b) 30 m made of nine elements. The elements outside this area are not visualised.

et al., 2006). The three element thick layer has a Young's modulus E =5, 1 and 0.125 GPa, in contrast to the stiffer surrounding having E =15 GPa. The element resolution outside the fault area is 50 m in X- and Z-direction and 500 m in the Y-direction.

170   The stress magnitudes along the profile (Fig. 9) do not show a significant stress variability in the vicinity of the fault resulting from the less stiff elements. Stress changes are restricted to the very narrow domain, which are not visible; they are visually hidden behind the fault line. S_{Hmax} decreases depending on the stiffness. For the model with E =250 MPa fault representation, S_{Hmax} is always around 1 MPa lower because of stress dissipation by the low stiff fault domain. Therefore, the von Mises stress drops by the same amount. Stress dissipation also effects S_{hmin}, but with a much lower amount; for S_V no effect is visible.

175   Another model version has a thicker fault representation by 30 m, made from nine elements (Fig. 8 b). Like the 10 m models, S_{Hmax} drops especially for the model with the least stiff fault domain (E =250 MPa) by around -3 MPa (Fig. 10), again an effect of the stress dissipation. S_{hmin} decreases by almost 1 MPa, whereas S_V is stable. Near the fault, S_{Hmax}, S_{hmin} and S_V decreases significant, limited to a region, narrow to the fault (<100 m). The von Mises stress variation is mainly driven by the reduction of S_{Hmax} because of the less stiff fault parts. There is no change of the S_{Hmax} orientation to observe; it is stable 180   parallel to the X-direction.

3.4   3-D-fault representation by elements with elasto-plastic rheology

As purely elastic elements do not allow failure, elements with elasto-plastic rheology within the fault zone are now used. Out of a continuous mesh, elements close to the fault location were selected in a staircase-like manner, which have a specific plastic yield criterion. These fault elements have laterally a range of one (Fig. 11 a) to eight elements (Fig. 11 b). These elements 185   have a friction angle of $\phi = 30°$ (friction coefficient $\mu = 0.58$) and a low cohesion of $C = 0.1$ kPa. The used dilatation angle is
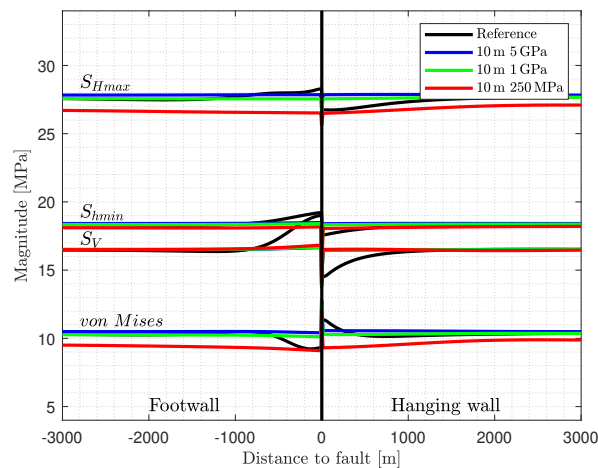
Figure 9. Fault representation by a 10 m thin layer of three weak elements. The fault elements have a lower Young's modulus (E =5, 1 and 0.125 GPa) in contrast to area outside this region (E =15 GPa). Shown in black is the reference model, and vertically the implemented fault.
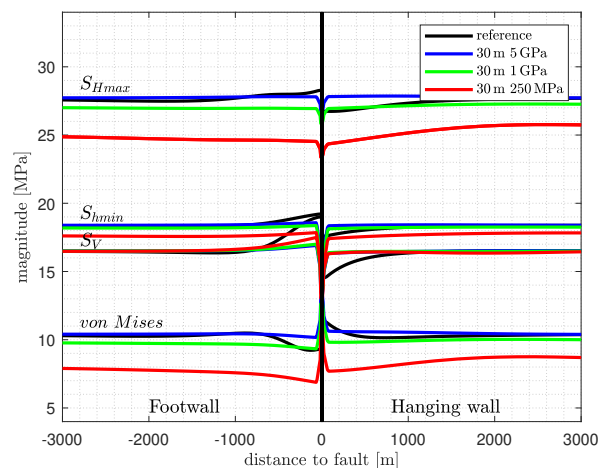
Figure 10. Fault representation by 30 m (nine elements) of elastic weak elements having a lower Young's modulus (E =5, 1 and 0.125 GPa), compared to the area outside this region with E =15 GPa. Shown in black is the reference model using contact surfaces, in colours are the model results with the less stiff 3-D-fault representation.

$\psi = 25°$. In contrast to that, the non-fault elements have a much larger cohesion ($C = 500$ kPa), but same friction- and dilation angle. The element resolution in the vicinity of the fault is 100 m in X- and Z-direction, and 500 m in the Y-direction. The elastic material properties are the same as used by the reference model ($E = 15$ GPa, $\nu = 0.27$ and $\rho = 2550$ kg m^{-3}).
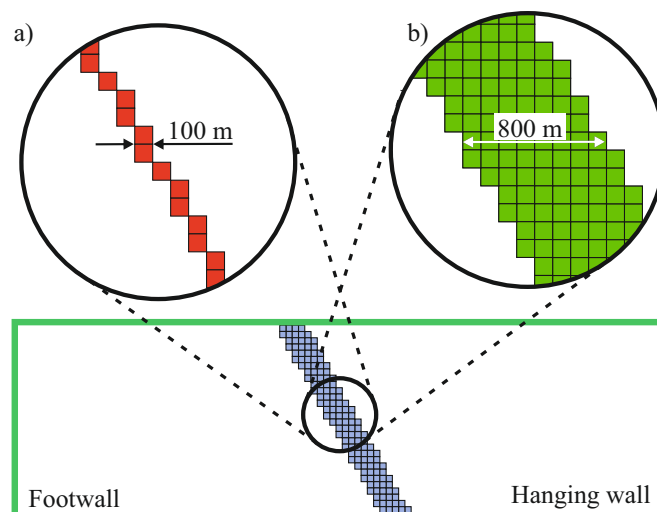
Figure 11. Sketch showing the fault representation by selected elements out of the mesh, which plastify as a result of friction and a low cohesion of $C = 0.1\,\text{kPa}$. Elements outside this region have a cohesion of $C = 500\,\text{kPa}$, the white area, where the mesh is not shown. A friction angle $\phi = 30°$ (friction coefficient $\mu = 0.58$) is used for all elements. Different number of lateral elements, representing the fault are tested, ranging from one (a) to eight (b) lateral elements. As the element size is $100\,\text{m}$ near the fault, the total with of the stair-step like fault ranges from 100 to $800\,\text{m}$.

The representation by means of staircase-like elements with elasto-plastic properties (Fig. 12) shows that the impact on the
190   stress components is nearly independent from the amount of laterally used elements that allow plastification. S_{Hmax}, S_{hmin}, S_{V} rises a little bit in the footwall block near the fault domain and is a little bit lower in the hanging wall block, again near the fault domain. The overall variation of S_{Hmax}, S_{hmin}, S_{V} and the von Mises is $<1\,\text{MPa}$. Stress magnitudes do not show any discontinuous behaviour at the fault, as the reference model do. Stress variations are restricted to a zone less than $1.500\,\text{m}$ to the fault domain. Again, the S_{Hmax} orientation is not disturbed as a result of the fault.

195   The model having laterally four weak elements is used again to investigate the impact of the friction angle (ϕ). Fig. 13 shows the result, where a friction angle of $\phi =$30, 25, 20 and 15° is applied. The $\phi =$30° model has already been used for the variation of the number of lateral elements (Fig. 12: 4 Elements). Modelling results in Fig. 13 show, that a decreasing friction angle increases the stress variation near the fault. S_{Hmax}, S_{hmin}, S_{V} rises in the footwall block near the fault, where a slight decrease can be seen in the hanging wall block. However, swing-in effects can be observed on both sides of the fault. Largest
200   magnitude changes are about $+4.5\,\text{MPa}$ for S_{V}, $+5\,\text{MPa}$ for S_{Hmax} and $+2.5\,\text{MPa}$ for S_{hmin}. In a distance of $>1400\,\text{m}$, to the fault centre, the variation of the stresses is $<1\,\text{MPa}$. The S_{Hmax} orientation keeps unaffected.

3.5   Variation of the fault dip angle

To study the impact of the fault dip angle, several models with different fault inclination are prepared. These models have an dip angle of 30, 40, 50, 70 and 80°, in contrast to the reference model (60°, Fig. 3). Elastic material properties are the same
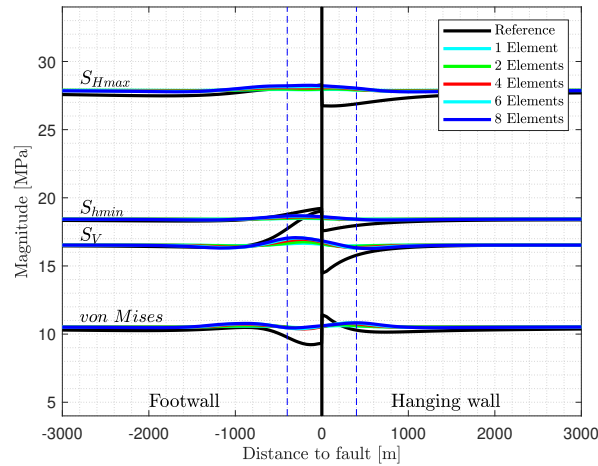
Figure 12. Fault representation with staircase-like elements with elasto-plastic rheology (Fig. 11) that are allowed to deform non-elastic. Shown in black is the reference model with the implemented fault, in colours are the models with a continuous mesh with the one (light blue) to eight lateral elements (dark blue). These elements have a low cohesion of $C = 0.1\,\mathrm{kPa}$ and a friction angle of $\phi = 30°$ (friction coefficient $\mu = 0.58$). The maximum width of eight elements is visualised by the dashed blue lines.
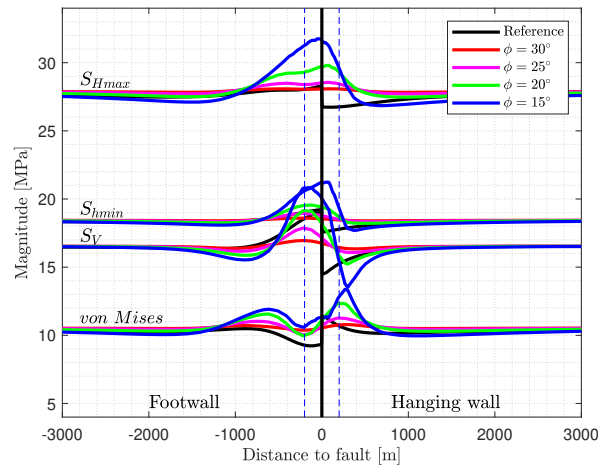
Figure 13. Fault representation with four staircase-like elements with elasto-plastic rheology (Fig. 11) that are allowed to deform non-elastic. Shown in black is the reference model and the implemented fault (vertical), in colours are the models with a friction angle of $\phi =$30, 25, 20 and 15°. The $\phi = 30°$ model is the same as the four Element model in Figure 12. The width of four elements is visualised by the blue dashed lines.

205   as used by the reference model: E=15 GPa, ν =0.27, ρ =2550 kg m^{-3} and fault representation by contact elements: μ =0.4 and C =0.
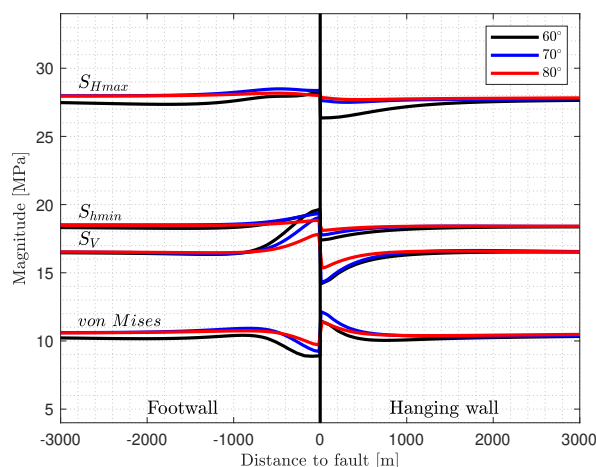
Figure 14. Influence of the dip angle of the fault on the stress components S_V, S_{Hmax}, S_{hmin} and the von Mises stress. Shown are the models with a fault dip angle of $60°$ (reference model), $70°$ and $80°$. By increasing the dip angle, the magnitude of stress perturbation decreases.
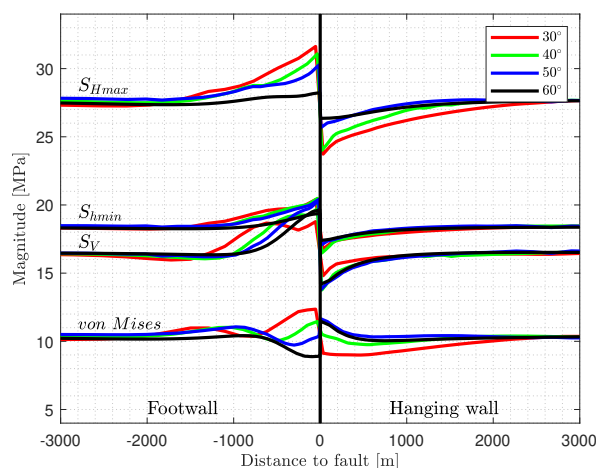
Figure 15. Influence of the fault dip angle on the stress components. A range of 60 (reference model), 50, 40 and $30°$ of the fault dip angle is shown. By reducing the dip angle, the stress magnitude change and the distance of the lateral stress perturbation increases. The most pronounced stress perturbation is seen for shallow dipping faults ($30°$ in red).

In Fig. 14, it can be seen that the stress perturbation pattern is similar compared to the reference mode. With increasing dip angle from $60°$ (reference model) to 70 and $80°$, the stress perturbation slightly decreases. The reduction is most significantly visible for the S_V magnitude in the footwall block next to the fault. Stress magnitudes away from the fault increase slightly for

210 the large dip angle models, as the stress dissipation by the fault decreases.

A decrease in dip angle of the fault results in a significantly more pronounced increase of the stress perturbation near the fault (Fig. 15). This leads to an increase of S_{Hmax} by >4 MPa in the footwall block, and a decrease of about -4 MPa in the hanging wall block, using an fault inclination of 30°. There is also a clear influence of the fault on the S_{Hmax} magnitude on both, the footwall and hanging wall block, in a distance to the fault of about 1.500 m and 2.000 m. An increase of the S_V and

215   S_{hmin} magnitudes in the footwall block and a decrease in the hanging wall block is clearly visible. There is no perturbation of the S_{Hmax} orientation.

3.6   Variation fault strike angle

In addition to the influence of the dip, the influence of the S_{Hmax} orientation with respect to that of the fault strike is investigated. Thus, an strike angle of 90° as the reference model is compared with other models where the fault is striking with an angle

220   of 70, 45, 30 and 15°. In order to allow geometrically such strike angles, the models are extended in the X-direction from 10 km to 20, 30 and 50 km for the 45, 30 and 15° models, respectively. The resulting boundary conditions are adapted, to allow comparability.

Results of the strike angle variation (Fig. 16) are shown parallel to the shortening direction S_{Hmax} and not perpendicular to the strike of the fault. The impact of the fault strike variation on the S_{Hmax} and S_{hmin} magnitude is minimal. Clear deviations

225   to the reference model are only for S_V in the footwall block. However, next to the fault, S_V is smaller for these models as the reference model. For the 15, 30 and 45° strike model, the S_V magnitude is significant larger up to 2.500 m away from the fault. But this distance is parallel to the main shortening direction. The distance normal to the contact is about 650 m.
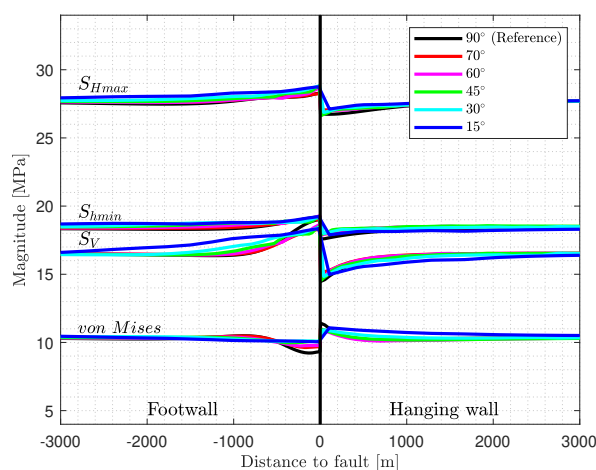
Figure 16. Variation of the strike angle, relative to the orientation of the maximum shortening. In contrast to the reference model with a fault strike angle of 90°, the varied models have a strike angle of 70, 60, 45, 30 and 15°. The stress components are plotted parallel to the shortening direction and not perpendicular to the fault.

As the fault strike is not perpendicular to the maximum compression for the horizontal stress orientation, deviation of S_{Hmax} occur from the orientation of the reference model, where S_{Hmax} is always $0°$. The angular variation of the S_{Hmax} orientation

230 varies with distance to the fault, but does not exceed $1.5°$. This value should be taken with caution in the near-field ($<100\,\text{m}$) to the fault, as the element resolution is not chosen to investigate the stress pattern next to the fault.

3.7 Young's Modulus

Since the elastic material properties have a significant influence on the deformation of the rock of both sides of the fault, the Young's modulus was varied. In addition to the Young's modulus of the reference model ($E = 15\,\text{GPa}$), stiffnesses of 5, 20,

235 30, 40, 60, 80 and $100\,\text{GPa}$ are tested. In order to make the model comparable, the boundary conditions are adopted (Tab. 2), so that the far-field stress magnitudes of the different models were equal.

Table 2. Boundary conditions are chosen depending on the Young's modulus to generate equal far-field stress magnitudes for the different models. The boundary conditions for $15\,\text{GPa}$ are the reference model settings.

Young's Modulus	X-shortening	Y-dilation
[GPa]	[m]	[m]
5	30.000	6.000
15	10.000	2.000
20	7.500	1,500
30	5.000	1.000
40	3.750	0.750
60	2.500	0.500
80	1.875	0.375
100	1.500	0.300

The variation of Young's modulus has limited effect on S_{Hmax} in the footwall block (Fig. 17), where in the hanging wall block S_{Hmax} decreases up to $-4\,\text{MPa}$ with increasing Young's modulus next to the fault. S_{hmin} increases slightly with the Young's modulus in the footwall block, and decreases in the same way in the hanging wall block slightly, up to $-2\,\text{MPa}$. The

240 S_{V} magnitude shows the same pattern, but the stress deviation is much larger near the fault, up to $+7\,\text{MPa}$ in the footwall and $-4.5\,\text{MPa}$ in the hanging wall block. The von Mises stresses decrease with increasing Young's modulus in the footwall block next to the fault and increases in the hanging wall block next to the fault.

In general, the stress perturbation increases due to a larger Young's modulus. The lateral influence of the fault on the stress components, producing a stress variation of more than $1\,\text{MPa}$, is limited to a range from $-1.000\,\text{m}$ to $+1.000\,\text{m}$ next to the

245 fault. Again, the S_{Hmax} orientation is always parallel to the direction of principal shortening.
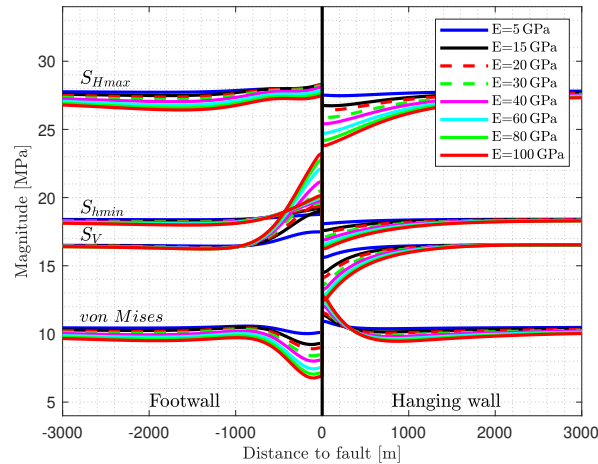
Figure 17. The influence of the Young's modulus on the stress perturbation is investigated. The models have a Young's modulus of $E =$ 5, 15 (reference model), 20, 30, 40, 60, 80 and 100 GPa.
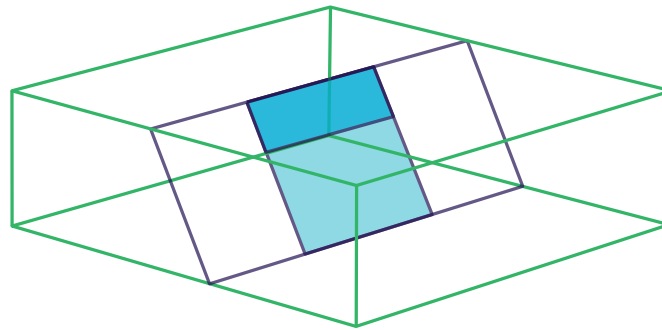
Figure 18. Model sketch with a reduced fault surface area of 4×3 km (light and dark blue areas together) and 4×1 km size (dark blue area only). Everything else is just the same as shown by Fig. 3.

3.8 Model size

It is obvious that the influence of the fault on the stress state also depends on the size of the fault surface or on the overall size of the model. For this purpose, the size of the active fault surface using the reference model geometry was reduced to a size of 4.000×1.000 m^2 and 4.000×3.000 m^2 (Fig. 18). Also, the reference model with the full fault surface was also doubled and quadrupled in size. The resulting models then have dimensions of 20×20×6 km^3 and 40×40×12 km^3, respectively. The resulting mesh resolution was then 100 m and 200 m in the X- and Z-directions, respectively, and 1 and 2 km in the strike direction (Y) of the fault, which is parallel to S_{hmin}. The boundary condition was adjusted accordingly, to generate a similar stress state.
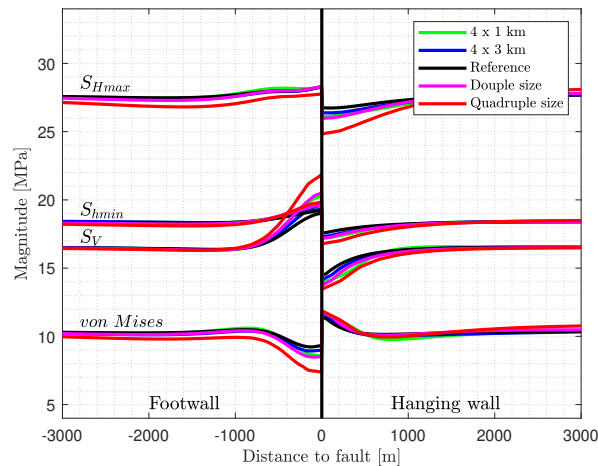
Figure 19. Influence of the fault size on the stress components. Models with a reduced fault surface area with a size of $4{\times}3\,\mathrm{km}^2$ and $4{\times}1\,\mathrm{km}^2$ (Fig. 18), as well as models like the reference model with a total size of $20{\times}20{\times}6\,\mathrm{km}^3$ (double size) and $40{\times}40{\times}12\,\mathrm{km}^3$ (quadruple size) are shown.

The comparison of the results in Fig. 19 shows that as the size of the fault increases, the magnitude deviation near the fault
255 increases. Thus, in the footwall block S_{Hmax} is reduced by almost $-3\,\mathrm{MPa}$, while S_V in the hanging wall block is increases by more than $+5\,\mathrm{MPa}$ for the model with side length of $40\,\mathrm{km}$. As a result, the von Mises stress in the footwall block decreases more significantly close to the fault. However, the increase of the fault surface area does not have a significant influence on the far-field stress pattern. Significant stress changes (>1 MPa) occur up to about $1.000\,\mathrm{m}$ next to the fault.

3.9 Strain variation

260 The effect of stress anisotropy is studied by defining variable lateral boundary conditions. The shortening, perpendicular to the fault strike (X-direction) is tested from 1, 2, 3, 4, 6, 8, 10 (reference model), 12, 14, 16 and $20\,\mathrm{m}$ ($\epsilon = -1*10^{-4}$ to $-2*10^{-3}$), where the dilation to the fault (Y-direction) remains identical to the reference model of $-2\,\mathrm{m}$ ($\epsilon = 2*10^{-4}$). Everything else is identical to the reference model.

The different S_{Hmax} magnitudes result directly from the variable shortening, applied to the model boundaries (Fig. 20). The
265 overall pattern is like the reference model. The observed variation is low for low strain, where variation is larger for higher strain. S_{Hmax} is smaller than the average away from the fault and rises next to the fault. In the footwall block, the pattern is clear: the closer to the fault, the smaller is S_{Hmax}.

The variation of S_{hmin} is similar to S_{Hmax}, variation is small for less shortening and rises by increasing shortening of the model (Fig. 20). S_{hmin} increases in the footwall block next to the fault and is smaller next to the fault in the hanging wall block.
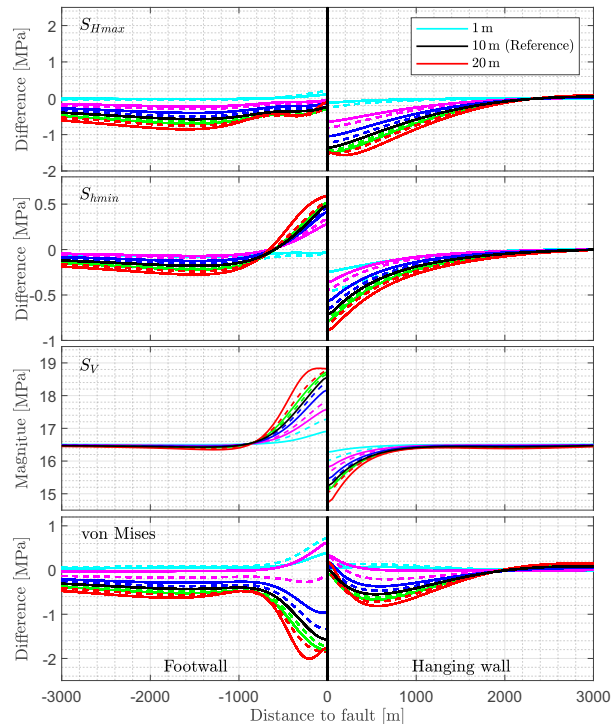
Figure 20. Influence of a variable strain on the stress components are shown. The models have a shortening of 1, 2, 3, 4, 6, 8, 10 (reference), 12, 14, 16 and 20 m (ϵ = -1*10^{-4} to $-2*10^{-3}$) perpendicular to the strike of the fault (X-direction) and a constant dilation of 2 m (ϵ =2*10^{-4}) parallel to the fault (Y-direction). Avoiding an overload on the legend, only the 1, 10 and 20 m model are indicated there. As the different lateral strain along the model boundaries result in different stress magnitudes, only the relative stress changes (local stresses - far field stress) are shown for S_{Hmax}, S_{hmin} and the von Mises stress. The general pattern of stress variation is like the reference model, the variation is smaller for lesser strain and larger for more strain. However, relative variation of the stress components are not bigger as about 1 MPa for S_{Hmax}, S_{hmin}, around 2 MPa for the von Mises stress and about 2.3 MPa for S_V.

270 Larger variation can be seen for S_V, with an increase in the footwall bock and a decrease in the hanging wall block. The S_V magnitude variation increases from 0.4 MPa for 2 m of shortening to 2.3 MPa for 20 m of shortening. Nearly the similar amount of decrease happens in the hanging wall block.

The von Mises stress variation (Fig. 20) increases with the rise of shortening compared to the reference model. For the model with little strain the observed variation of the von Mises stress displays another pattern. For them, the von Mises stress increases 275 in the footwall block a decrease in the hanging wall block, next to the fault. Again, major stress variations are restricted for a distance of less than 1.000 m next to the fault. S_{Hmax} orientation is not affected for larger shortening perpendicular to the fault. For the models with a shortening of 1 and 2 m of shortening in the X-direction, under an dilation of 2 m in the Y-direction, there is no clear S_{Hmax} orientation anymore, it becomes chaotic (not shown).
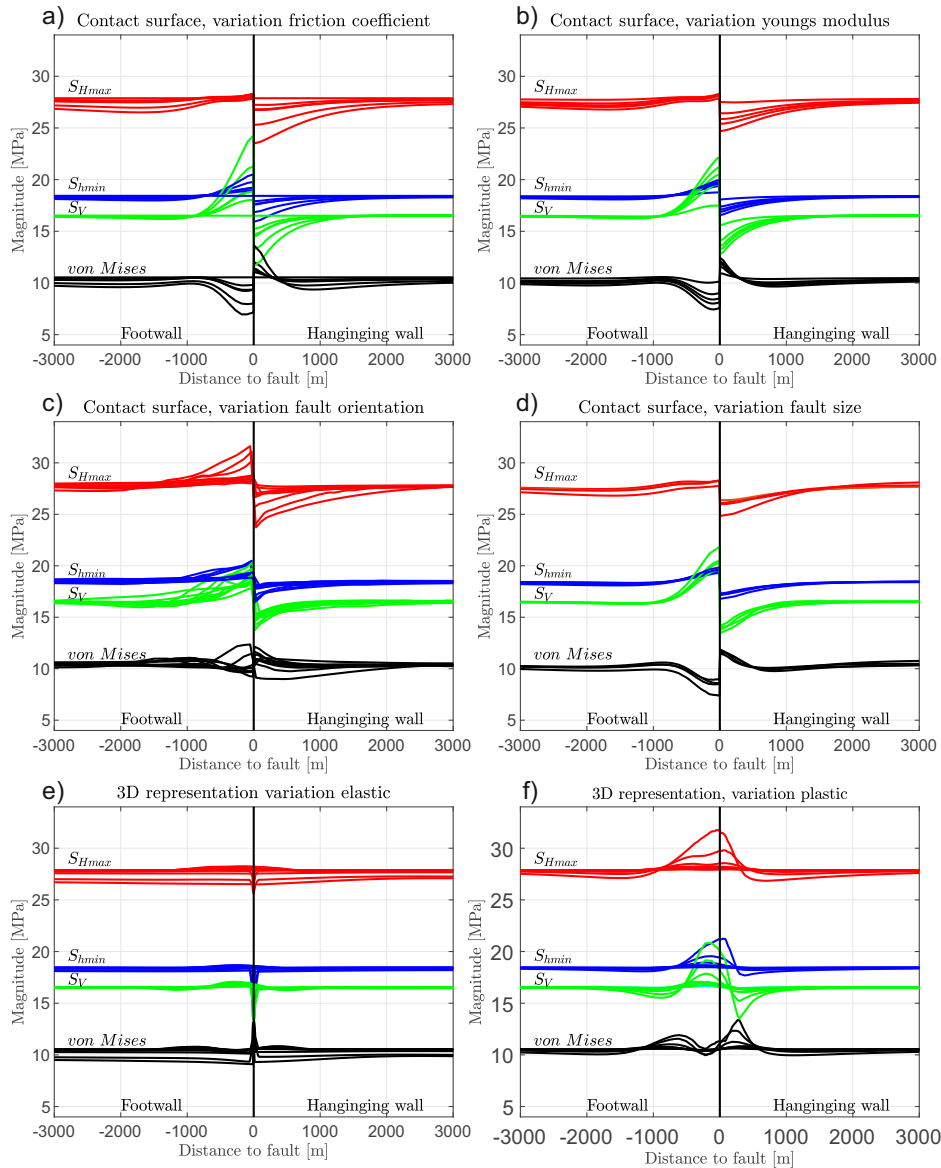
Figure 21. Summary illustration of the results from various presented models. Subfigure a) shows the impact of the fault friction using contact elements (Fig. 7), b) displays the influence of a variable Young's modulus of the host rock on the stress state near and far the fault (Fig. 17). Subfigure c) shows the impact of a variable fault dip and a variable fault strike on the stress state resulting from a fault represented by a contact surface (Figs. 15, 14 and 16), where d) illustrates the influence of the fault size and model size (Fig. 19). The impact of a fault representation by 3-D elements is shown, where d) elastically weak elements are with a different stiffness (Figs. 9 and 10) and e) where the elements are allow to plastifiy as a result of a variable low friction (Fig. 13) and a laterally variable amount of elements (Fig. 12).

4 Discussion

4.1 Model simplification

Simple numeric models are generated, where different geometries, technical approaches and different material properties are used to represent a fault or a fault zone. The goal is to investigates the impact of faults on the far field stress state (>100 m). The model design does not allow estimations on the stress state or stress perturbations close to a fault (<100 m). Investigating that, a much finer mesh resolution would be needed.

Like all generic models, those ones used here are a strong simplification of rock physics, geological structures, and the fault representation itself. Except for two scenarios, only linear elastic material properties are used to represent the rock volume. This neglects various rheological processes within the Earth's crust. But Hooke's law seems to be a proper approximation for the major mechanical behaviour of rocks in the upper crust, as the elastic thickness of the crust (T_e) is usually much larger than the models used here (Burov and Diament, 1995; Hyndman et al., 2009; Tesauro et al., 2012). According to field investigations by Maerten et al. (2016), most brittle deformation can be explained using linear elastic material properties. Furthermore, the focus is not on stress changes during the co-seismic phase (e.g., Brodsky et al., 2020; Lin et al., 2013; Shi et al., 2020; Zhang and Ma, 2021), or deformation over several seismic cycles. The focus is on the quasi-static stress state in the inter-seismic phase.

To allow good comparability of modelling results, constant boundary conditions has been used, with a few exceptions. The models with different strain have of course different stress magnitudes as a result. For models having a different extend or a variable Young's modulus, the boundary conditions were scaled accordingly to ensure comparability. The models with a lower Young's modulus in the fault zone dissipate localised stresses, which has not been corrected, as the influence on the result are negligible.

4.2 Discontinuity approach: contact elements

Several of the model scenarios use contact elements to represent a fault within the model. This is the case for the reference model, the variation of the friction, the fault dip- and fault strike angle, the Young's modulus variation in the county rock, the model size and the boundary conditions. The overall observation is an increase of the stress components (S_{Hmax}, S_{hmin} and S_V) in the footwall block and a decrease within the hanging wall block, both next to the fault (Fig. 21 a-d). In contrast, the von Mises stresses decreases in the footwall block and increases in the hanging wall block. This is the case as S_V, which is mostly σ_3 varies more than the other stress components.

For these contact surfaces we assume no cohesion ($C =0$) which is a reasonable simplification in particular for pre-existing faults or fault zones, as granular material have a very low cohesion: $C < 1$ kPa (Schellart, 2000). On the other hand, cohesion strengthening can increase the cohesion to $C > 1$ MPa (van den Ende and Niemeijer, 2019), $C = 8$ MPa (Muhuri et al., 2003) or $C = 35$ MPa for very high temperatures (Tenthorey and Cox, 2006). According to Tenthorey and Cox (2006), cohesion will reach 3 MPa for an 100 years recurrence interval for a depth of about 2 km.

The used friction coefficient (μ) for the contact surfaces reaches from 0.1 over 0.4 (reference model) to 1.0 and larger. In the past, it was assumed, that the friction coefficient of faults is about 0.6 to 0.85 (Byerlee, 1978; Brace and Kohlstedt, 1980; Brudy et al., 1997). But the μ can be much smaller, if clay minerals dominate (Byerlee, 1978; Lockner et al., 2011), in the case of dynamic offset (Di Toro et al., 2011; Boulton et al., 2017) or for high pore pressures (Blanpied et al., 1992; Byerlee, 1993).

315 Low friction is also expected for large fault (zones) or subduction zones (Fulton et al., 2013; Bird and Xianghong Kong, 1994; Iaffaldano, 2012; Carena and Moder, 2009; Carpenter et al., 2015; Houston, 2015). The friction coefficient is in the order of 0.08 for the 2011 Tohoku-Oki Earthquake (Fulton et al., 2013), $\mu = 0.12$–0.25 or 0.05–0.2 for the San Andreas Fault (Bird and Xianghong Kong, 1994; Carena and Moder, 2009) or for tremors in general $\mu = 0$ to 0.1 (Houston, 2015). Iaffaldano (2012) assumes a friction coefficient of 0.01 to 0.07 for large scale plate boundaries. However, the investigated range of μ cover

320 this variation well, except for $\mu < 0.1$.

As a free surface, or a fault with very low friction coefficient, is unable to build up shear stresses (Hafner, 1951), principal stresses will be parallel and perpendicular to the surface (Camac and Hunt, 2009; Bell, 1996; Hudson and Cooling, 1988; Osokina, 1988; Petit and Mattauer, 1995; Rawnsley et al., 1992). A classic example is the San Andreas Fault (Mount and Suppe, 1987), where the interpretation of borehole breakouts and drilling induced tensile fractures from near-by borehole indicate in

325 S_{Hmax} orientations that are almost perpendicular to the fault (Mount and Suppe, 1992; Zoback et al., 1987). However, the distance of these boreholes is $>1.000\,\mathrm{m}$ in most cases and thus it is questionable that the derived S_{Hmax} orientations can be used as an observable for the fault strength.

4.3 Continuity approach: Weak elements as fault zone

4.3.1 Young's modulus variation in the fault zone

330 Fault representation by elastic weak elements exhibits no significant stress variation pattern using three elements (Figs. 10 compared to the reference model using contact elements. Even, if the number of elements representing the fault zone is increased to nine, the stress pattern is hardly different (Fig. 10). Only narrow to the fault, a stress drop can be observed for S_{Hmax}, S_{hmin} and S_{V}. The von Mises stress rises locally, as the S_{Hmax} decrease is lower than for S_{hmin} and S_{V}. Localised swing-in effects can be observed; from the extend, most probably an artefact of the mesh resolution.

335 Fault zones are a 3-D structure consisting of the fault core and the damage zone (Caine et al., 1996; Chester and Logan, 1986; Faulkner et al., 2003, 2006). Previous work suggests, that the Young's modulus of the host rock decreases towards the damage zone, where the Poisson's ratio increases in the same way (Faulkner et al., 2006; Casey, 1980; Isaacs et al., 2008). However, the variation of the Poisson's ratio is not tested here. Observed reduction of Young's modulus is from $55.4\,\mathrm{GPa}$ down to $16.2\,\mathrm{GPa}$ (Isaacs et al., 2008) or a reduction of about $6.5\,\mathrm{GPa}$, e.g., from $66\,\mathrm{GPa}$ to $59.5\,\mathrm{GPa}$ (Faulkner et al., 2006).

340 The here investigated range from $E = 15\,\mathrm{GPa}$ to $0.125\,\mathrm{GPa}$ covers a large material property range. According Treffeisen and Henk (2020a), the amount of Young's modulus contrast have a strong impact on the resulting stress perturbation. Overall, this method did not provide a stress pattern like the contact surface method. Therefore, the representation of a fault by elastic weak elements only is apparent rather a method to dissipate stresses, but not to represent low friction faults properly.

4.3.2   Friction within the 3-D elements

345   The models having a 3-D-representation of the fault with a lateral variable number of elements, are allowed to fail according to the Mohr-Coulomb-Criteria. The resulting stress state by a friction angle of $\phi =30°$ and a cohesion of $C =0.1$ kPa (Fig. 12) did not show much difference, compared to a model without a fault representation. Magnitude changes are in the order of less than 1 MPa next to the fault zone. The models with a lower friction displays lager stress perturbation in the vicinity of the fault (Fig. 13). The magnitude of stress perturbation is larger for the model using a friction angle of 15°, compared to the

350   reference model with contact surfaces. The overall pattern is complex, some of the trends are similar, but the stress magnitudes are not decoupled when crossing the fault zone. As previously discussed, a low friction can be assumed for present-day fault activity. However, resulting stress pattern differ to the results using contact elements. The continuous mesh did not allow a real decoupling. This is may be different for other methods such as DEM where resulting behaviour depends on the number of elements and the friction (Hunt et al., 2004).

355   ### 4.3.3   Cohesion variation within the 3-D elements

Usually, the key driver between intact rock and the fault using the Mohr-Coulomb-failure criteria is not the friction coefficient, but the cohesion. Even from the modelling perspective, cohesion have the largest impact (Treffeisen and Henk, 2020a) on the stress state. Therefore the models with elements with elasto-plastic rheology use the same friction ($\phi =30°$, or $\mu = 0.58$), but a very low cohesion $C =0.1$ kPa for the fault zone, in contrast of $C =500$ kPa outside this area. This is also the case for elements

360   with elasto-plastic rheology, even if the parallel number reaches eight elements.

4.4   Distance of Stress disturbance to faults

The impact of the different modelling approaches on the stress state differs. But a significant stress perturbation is spatially limited to a distance of maximum 1.000–1.500 m next to the fault. Fig. 21 provides an visual overview of modelling results. This major assumption is supported by several authors using different approaches from a more map-view perspective (Faulkner

365   et al., 2006; Petit and Mattauer, 1995; Provost and Houston, 2001; Su and Stephansson, 1999; Yale, 2003). Also, observations from wells support that, where the stress perturbation is usually <200 m away from the fault (Barton and Zoback, 1994; Brudy et al., 1997; Lin et al., 2010; Stephansson and Ångman, 1986; Tamagawa and Pollard, 2008). A rotation of about 90° within less than 100 to 200 m in the vicinity of a fault has been observed near the Taiwan Chelungpu-fault (Lin et al., 2010) or at the Lansjärv well (Sweden, Bjarnason et al., 1989).

370   The relative stress state affects the spatial stress perturbation (Pollard and Segall, 1987). Therefore, Yale (2003) assumes, that in the case of low differential stress, the spatial extend of stress perturbation is able to be observe for up to several kilometres away from the fault. This fits in general to the results of the models varying the lateral strain, where the stress magnitude variation near the faults increases with a larger differential stress. Some previous models show more spacious far-field stress perturbations (Camac and Hunt, 2009; Sánchez D. et al., 1999; Tommasi et al., 1995), which are most probably an artefact of

375   a too coarse mesh resolution.
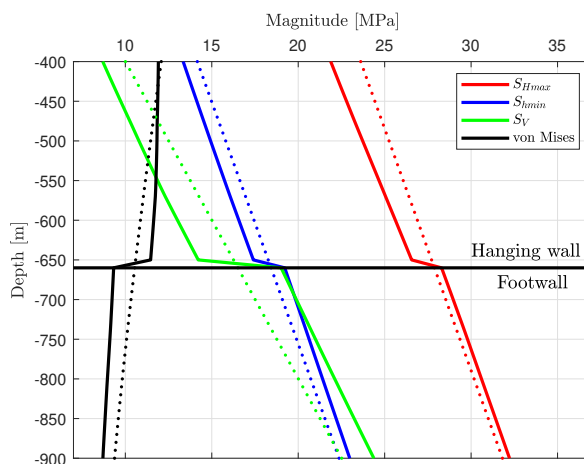
Figure 22. Stress magnitudes from a virtual well section for the depth range of 400 to 900 m depth, of the reference model having contact surfaces (continuous line) and a model without a fault (dotted line).
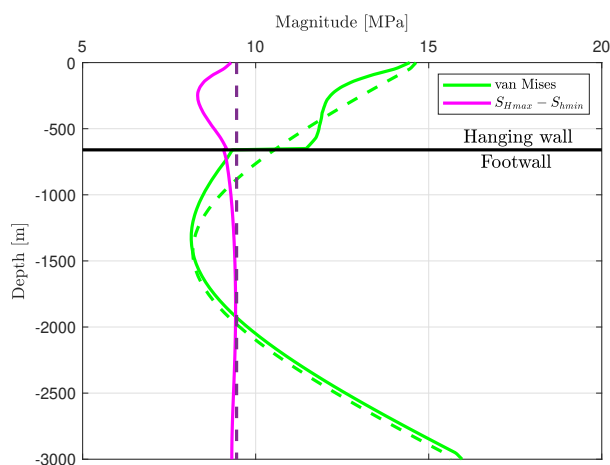
Figure 23. The von Mises and the difference between both horizontal stresses (S_{Hmax} - S_{hmin}) are shown for the reference model witch contact surfaces (continuous line) and a model with a continuous mesh (dotted line).

4.5 Magnitude of stress perturbation

A decrease of horizontal stresses near the faults in the hanging wall, and an increase in the footwall is reported for the Forsmark DBT 1 well (Sweden, Stephansson and Ångman, 1986). Less borehole breakouts in the hanging wall block and more in the footwall block are observed from the KTB well (Germany, Barton and Zoback, 1994). A reduction of σ_3 by about 5 MPa has been observed within less than 10 m near a tunnel at the Grimsel test site (Switzerland, Krietsch et al., 2019). All these

380

observations fit to the results of the models having a fault representation by contact elements, where the horizontal stresses are smaller above the fault (Fig. 22), and the horizontal differential stress is smaller in the hanging wall block (Fig. 23). The latter would make the occurrence of borehole breakouts less likely in the hanging wall.

385 In contrast to that, larger horizontal stresses above a fault have been observed for the Lansjärv well (Sweden, Bjarnason et al., 1989). The maximum horizontal stresses are observed about 100 m above the fault in the hanging wall block, which points also to other causes. One possible explanation is the lithological variation in the well, where several pegmatites and amphibolites in that depth range has been observed (Bjarnason et al., 1989), which eventually provide larger magnitudes as a result of a larger Young's modulus.

According to Su and Stephansson (1999) is the magnitude variation positive correlated with the stress ratio and negative
390 correlated with the friction. This can be clearly confirmed by this study (Figs. 7 and 20), where the stress variation near fault is largest for low friction models and models with a larger strain variation. Observation indicate that stresses decrease near a fault after an earthquake (Li et al., 2023; Zhou et al., 2012; Wang et al., 2015). This can be confirmed by the models for the hanging wall, but not for the footwall block. Either the observations are from the hanging wall block only, or other factors are responsible, which are not represented by the models, used here.

395 **4.6 Other potential factors**

Stress changes near the fault tip led to a complex stress pattern (Segall and Pollard, 1980; Rispoli, 1981; Homberg et al., 1997). To mimic that, using only linear elastic material properties would lead to wrong assumptions. Therefore, such structures are not considered here. However, it can be assumed that stress changes induced by fault tips are negligible at distances of a few kilometres from the fault (Segall and Pollard, 1980; Su and Stephansson, 1999).

400 Several other potential geometrical reasons of stress perturbation are not tested here. For example, the curvature (e.g., listric fault) or roughness of the fault. Fault zones can exist out of several single parallel faults, which probably would produce a wider distributed area of stress perturbation. Pore pressure, especially overpressure, can have a large potential on the stress state (Blanpied et al., 1992; Byerlee, 1993), significant impact on the fault behaviour. But this has not been tested here.

5 Conclusions

405 The results of our study show that the static fault friction coefficient, rock strength, stiffness and density contrast of the fault significantly affect the stress tensor beyond the fault core. However, the stress magnitudes as well as stress tensor orientation is not significantly changed beyond a distance of about 1.000 or 1.500 m. From these findings we can conclude that most of the stress tensor rotations that are documented in recent publications based on high density data sets (Heidbach et al., 2007; Lund Snee and Zoback, 2018, 2020; Pierdominici and Heidbach, 2012; Rajabi et al., 2016, 2017b) are very much likely not
410 controlled by faults, but rather rock property variability (e.g., Reiter, 2021), by superposition of plate boundary forces with different orientation and magnitude, or a mixture of both (Ferreira et al., 1998; Rajabi et al., 2017a).

Symbols

Table 3. Explanation of the symbols used

C	Cohesion
DEM	Discret Element Method
E	Youngs Modulus
FEM	Finite Element Method
g	Gravitational acceleration
S_{Hmax}	Maximum horizontal stress
S_{hmin}	Minimum horizontal stress
S_V	Vertical stress
X, Y, Z	Coordinates (cartesian)
z	Depth
ϵ	Strain
μ	Static friction coefficient
ν	Poisson's ratio
ρ	Density
σ	Stress tensor
σ_1	Largest principal stress
σ_2	Intermediate principal stress
σ_3	Least principal stress
σ_D	Differential stress
σ_{vM}	von Mises stress
ϕ	Friction angle
ψ	Dilation angle

Competing interests

The contact author has declared that none of the authors has any competing interests.

415 *Acknowledgements.* Some of the results of that study was first presented in Heidbach and Reiter (2019). This study was partly funded by the National Cooperative for the Disposal of Radioactive Waste (Nagra), Switzerland and the Bundesgesellschaft für Endlagerung (BGE) within the project SpannEnD II (www.spannend-projekt.de).

References

Anderson, E. M.: The dynamics of faulting, Transactions of the Edinburgh Geological Society, 8, 387–402, https://doi.org/10.1144/transed.8.3.387, 1905.

Anderson, E. M.: The Dynamics of Faulting and Dyke Formation with Application to Britain, 2nd ed. Oliver and Boyd, London and Edinburgh, 1951.

Barton, C. A. and Zoback, M. D.: Stress perturbations associated with active faults penetrated by boreholes: Possible evidence for near-complete stress drop and a new technique for stress magnitude measurement, Journal of Geophysical Research: Solid Earth, 99, 9373–9390, https://doi.org/10.1029/93JB03359, 1994.

Bell, J. S.: In situ stresses in sedimentary rocks (part 2): Applications of stress measurements, Geoscience Canada, 23, 135–153, http://journals.hil.unb.ca/index.php/GC/article/view/3910, 1996.

Bird, P. and Xianghong Kong: Computer simulations of California tectonics confirm very low strength of major faults, Geological Society of America Bulletin, 106, 159–174, https://doi.org/10.1130/0016-7606(1994)106<0159:CSOCTC>2.3.CO;2, 1994.

Bjarnason, B., Zellman, O., and Wikberg, P.: Drilling and borehole description, in: Interdisciplinary study of post-glacial faulting in the Lansjärv area Northern Sweden 1986 - 1988, edited by Bäckblom, G. and Stanfors, R., chap. 7, pp. 7:1–7:14, Svensk Kärnbränslehantering Aktiebolag (SKB), skb tr 89- edn., 1989.

Blanpied, M. L., Lockner, D. A., and Byerlee, J. D.: An earthquake mechanism based on rapid sealing of faults, Nature, 358, 574–576, https://doi.org/10.1038/358574a0, 1992.

Blöcher, G., Cacace, M., Jacquey, A. B., Zang, A., Heidbach, O., Hofmann, H., Kluge, C., and Zimmermann, G.: Evaluating Micro-Seismic Events Triggered by Reservoir Operations at the Geothermal Site of Groß Schönebeck (Germany), Rock Mechanics and Rock Engineering, 51, 3265–3279, https://doi.org/10.1007/s00603-018-1521-2, 2018.

Boulton, C., Yao, L., Faulkner, D. R., Townend, J., Toy, V. G., Sutherland, R., Ma, S., and Shimamoto, T.: High-velocity frictional properties of Alpine Fault rocks: Mechanical data, microstructural analysis, and implications for rupture propagation, Journal of Structural Geology, 97, 71–92, https://doi.org/10.1016/j.jsg.2017.02.003, 2017.

Brace, W. F. and Kohlstedt, D. L.: Limits on lithospheric stress imposed by laboratory experiments, Journal of Geophysical Research, 85, 6248, https://doi.org/10.1029/JB085iB11p06248, 1980.

Brodsky, E. E., Mori, J. J., Anderson, L., Chester, F. M., Conin, M., Dunham, E. M., Eguchi, N., Fulton, P. M., Hino, R., Hirose, T., Ikari, M. J., Ishikawa, T., Jeppson, T., Kano, Y., Kirkpatrick, J., Kodaira, S., Lin, W., Nakamura, Y., Rabinowitz, H. S., Regalla, C., Remitti, F., Rowe, C., Saffer, D. M., Saito, S., Sample, J., Sanada, Y., Savage, H. M., Sun, T., Toczko, S., Ujiie, K., Wolfson-Schwehr, M., and Yang, T.: The State of Stress on the Fault Before, During, and after a Major Earthquake, https://doi.org/10.1146/annurev-earth-053018-060507, 2020.

Brudy, M., Zoback, M. D., Fuchs, K., Rummel, F., and Baumgärtner, J.: Estimation of the complete stress tensor to 8 km depth in the KTB scientific drill holes: Implications for crustal strength, Journal of Geophysical Research: Solid Earth, 102, 18 453–18 475, https://doi.org/10.1029/96JB02942, 1997.

Buchmann, T. J. and Connolly, P. T.: Contemporary kinematics of the Upper Rhine Graben: A 3D finite element approach, Global and Planetary Change, 58, 287–309, https://doi.org/10.1016/j.gloplacha.2007.02.012, 2007.

Burov, E. B. and Diament, M.: The effective elastic thickness (Te) of continental lithosphere: what does it really mean?, Journal of Geophysical Research, 100, 3905–3927, https://doi.org/10.1029/94JB02770, 1995.

455 Byerlee, J.: Friction of Rocks, Pure and Applied Geophysics PAGEOPH, 116, 615–626, https://doi.org/10.1007/BF00876528, 1978.

Byerlee, J.: Model for episodic flow of high-pressure water in fault zones before earthquakes, Geology, 21, 303–306, https://doi.org/10.1130/0091-7613(1993)021<0303:MFEFOH>2.3.CO;2, 1993.

Caine, J. S., Evans, J. P., and Forster, C. B.: Fault zone architecture and permeability structure, Geology, 24, 1025, https://doi.org/10.1130/0091-7613(1996)024<1025:FZAAPS>2.3.CO;2, 1996.

460 Camac, B. A. and Hunt, S. P.: Predicting the regional distribution of fracture networks using the distinct element numerical method, AAPG Bulletin, 93, 1571–1583, https://doi.org/10.1306/07230909040, 2009.

Cappa, F.: Modelling fluid transfer and slip in a fault zone when integrating heterogeneous hydromechanical characteristics in its internal structure, Geophysical Journal International, 178, 1357–1362, https://doi.org/10.1111/j.1365-246X.2009.04291.x, 2009.

Cappa, F. and Rutqvist, J.: Impact of CO2 geological sequestration on the nucleation of earthquakes, Geophysical Research Letters, 38, 2–7,
465 https://doi.org/10.1029/2011GL048487, 2011.

Carena, S. and Moder, C.: The strength of faults in the crust in the western United States, Earth and Planetary Science Letters, 287, 373–384, https://doi.org/10.1016/j.epsl.2009.08.021, 2009.

Carpenter, B. M., Saffer, D. M., and Marone, C.: Frictional properties of the active San Andreas Fault at SAFOD: Implications for fault strength and slip behavior, Journal of Geophysical Research: Solid Earth, 120, 5273–5289, https://doi.org/10.1002/2015JB011963, 2015.

470 Casey, M.: Mechanics of shear zones in isotropic dilatant materials, Journal of Structural Geology, 2, 143–147, https://doi.org/10.1016/0191-8141(80)90044-9, 1980.

Chéry, J., Zoback, M. D., and Hickman, S.: A mechanical model of the San Andreas fault and SAFOD Pilot Hole stress measurements, Geophysical Research Letters, 31, 1–6, https://doi.org/10.1029/2004GL019521, 2004.

Chester, F. M. and Logan, J. M.: Implications for mechanical properties of brittle faults from observations of the Punchbowl fault zone,
475 California, Pure and Applied Geophysics, 124, 79–106, https://doi.org/10.1007/BF00875720, 1986.

Cundall, P. A. and Hart, R. D.: Numerical Modelling of Discontinua, Engineering Computations, 9, 101–113, https://doi.org/10.1108/eb023851, 1992.

Dart, R. L. and Swolfs, H. S.: Subparallel faults and horizontal-stress orientations: An evaluation of in-situ stresses inferred from ellipti-cal wellbore enlargements, Norwegian Petroleum Society Special Publications, 1, 519–529, https://doi.org/10.1016/B978-0-444-88607-
480 1.50041-3, 1992.

Desroches, J., Peyret, E., Gisolf, A., Wilcox, A., Giovanni, M. D., de Jong, A. S., Sepehri, S., Garrard, R., and Giger, S.: Stress Measurement Campaign in Scientific Deep Boreholes: Focus on Tool and Methods, in: SPWLA 62nd Annual Logging Symposium, https://doi.org/10.30632/spwla-2021-0056, 2021.

Di Toro, G., Han, R., Hirose, T., De Paola, N., Nielsen, S., Mizoguchi, K., Ferri, F., Cocco, M., and Shimamoto, T.: Fault lubrication during
485 earthquakes, Nature, 471, 494–499, https://doi.org/10.1038/nature09838, 2011.

Faulkner, D. R., Lewis, A. C., and Rutter, E. H.: On the internal structure and mechanics of large strike-slip fault zones: Field observations of the Carboneras fault in southeastern Spain, Tectonophysics, 367, 235–251, https://doi.org/10.1016/S0040-1951(03)00134-3, 2003.

Faulkner, D. R., Mitchell, T. M., Healy, D., and Heap, M. J.: Slip on 'weak' faults by the rotation of regional stress in the fracture damage zone, Nature, 444, 922–925, https://doi.org/10.1038/nature05353, 2006.

490 Ferreira, J. M., Oliveira, R. T., Takeya, M. K., and Assumpção, M.: Superposition of local and regional stresses in northeast Brazil: evidence from focal mechanisms around the Potiguar marginal basin, Geophysical Journal International, 134, 341–355, https://doi.org/10.1046/j.1365-246X.1998.00563.x, 1998.

Ferrill, D. A., Smart, K. J., and Morris, A. P.: Fault failure modes, deformation mechanisms, dilation tendency, slip tendency, and conduits v. Seals, Geological Society Special Publication, 496, 75–98, https://doi.org/10.1144/SP496-2019-7, 2020.

495 Fitzenz, D. D. and Miller, S. A.: A forward model for earthquake generation on interacting faults including tectonics, fluids, and stress transfer, Journal of Geophysical Research: Solid Earth, 106, 26 689–26 706, https://doi.org/10.1029/2000jb000029, 2001.

Franceschini, A., Ferronato, M., Janna, C., and Teatini, P.: A novel Lagrangian approach for the stable numerical simulation of fault and fracture mechanics, Journal of Computational Physics, 314, 503–521, https://doi.org/10.1016/j.jcp.2016.03.032, 2016.

Fuchs, K. and Müller, B.: World Stress Map of the Earth: a key to tectonic processes and technological applications, Naturwissenschaften,
500 88, 357–371, https://doi.org/10.1007/s001140100253, 2001.

Fulton, P. M., Brodsky, E. E., Kano, Y., Mori, J., Chester, F., Ishikawa, T., Harris, R. N., Lin, W., Eguchi, N., and Toczko, S.: Low coseismic friction on the Tohoku-Oki fault determined from temperature measurements, Science, 342, 1214–1217, https://doi.org/10.1126/science.1243641, 2013.

Hafner, W.: Stress distributions and faulting, Bulletin of the Geological Society of America, 62, 373–398, https://doi.org/10.1130/0016-
505 7606(1951)62[373:SDAF]2.0.CO;2, 1951.

Hardebeck, J. L. and Okada, T.: Temporal Stress Changes Caused by Earthquakes: A Review, Journal of Geophysical Research: Solid Earth, 123, 1350–1365, https://doi.org/10.1002/2017JB014617, 2018.

Heidbach, O. and Ben-Avraham, Z.: Stress evolution and seismic hazard of the Dead Sea Fault System, Earth and Planetary Science Letters, 257, 299–312, https://doi.org/10.1016/j.epsl.2007.02.042, 2007.

510 Heidbach, O. and Reiter, K.: Interner Bericht NIB 19-15 - Impact of fault properties and fault implementation strategies on results of 3D geomechanical-numerical models, Tech. Rep. March, NAGRA, Wettingen, 2019.

Heidbach, O., Barth, A., Connolly, P. T., Fuchs, K., Müller, B., Tingay, M., Reinecker, J., Spencer, B., and Wenzel, F.: Stress Maps in a Minute: The 2004 World Stress Map Release, Eos, Transactions American Geophysical Union, 85, 521, https://doi.org/10.1029/2001GC000252.Fuchs, 2004.

515 Heidbach, O., Reinecker, J., Tingay, M., Müller, B., Sperner, B., Fuchs, K., and Wenzel, F.: Plate boundary forces are not enough: Second- and third-order stress patterns highlighted in the World Stress Map database, Tectonics, 26, 1–19, https://doi.org/10.1029/2007TC002133, 2007.

Heidbach, O., Rajabi, M., Cui, X., Fuchs, K., Müller, B., Reinecker, J., Reiter, K., Tingay, M., Wenzel, F., Xie, F., Ziegler, M. O., Zoback, M.-L., and Zoback, M. D.: The World Stress Map database release 2016: Crustal stress pattern across scales, Tectonophysics, 744, 484–498,
520 https://doi.org/10.1016/j.tecto.2018.07.007, 2018.

Henk, A.: Numerical modelling of faults, in: Understanding Faults, chap. 4, p. 2, Elsevier, https://doi.org/10.1016/b978-0-12-815985-9.00004-7, 2020.

Hergert, T. and Heidbach, O.: Geomechanical model of the Marmara Sea region-II. 3-D contemporary background stress field, Geophysical Journal International, 185, 1090–1102, https://doi.org/10.1111/j.1365-246X.2011.04992.x, 2011.

525 Hergert, T., Heidbach, O., Bécel, A., and Laigle, M.: Geomechanical model of the Marmara Sea region-I. 3-D contemporary kinematics, Geophysical Journal International, 185, 1073–1089, https://doi.org/10.1111/j.1365-246X.2011.04991.x, 2011.

Hergert, T., Heidbach, O., Reiter, K., Giger, S. B., and Marschall, P.: Stress Field Sensitivity Analysis at a Reservoir Scale (Northern Switzerland) Using Numerical Geomechanical Modelling, Solid Earth, 6, 533–552, https://doi.org/10.5194/se-6-533-2015, 2015.

Hickman, S. and Zoback, M.: Stress orientations and magnitudes in the SAFOD pilot hole, Geophysical Research Letters, 31, L15S12,
530 https://doi.org/10.1029/2004GL020043, 2004.

Homberg, C., Hu, J., Angelier, J., Bergerat, F., and Lacombe, O.: Characterization of stress perturbations near major fault zones: insights from 2-D distinct-element numerical modelling and field studies (Jura mountains), Journal of Structural Geology, 19, 703–718, https://doi.org/10.1016/S0191-8141(96)00104-6, 1997.

Houston, H.: Low friction and fault weakening revealed by rising sensitivity of tremor to tidal stress, Nature Geoscience, 8, 409–415, https://doi.org/10.1038/ngeo2419, 2015.

Hudson, J. A. and Cooling, C. M.: In Situ rock stresses and their measurement in the U.K.-Part I. The current state of knowledge, International Journal of Rock Mechanics and Mining Sciences and, 25, 363–370, https://doi.org/10.1016/0148-9062(88)90976-X, 1988.

Hunt, S. P., Camac, B. A., and Boult, P.: A parametric analysis and applications of the discrete element method for stress modeling, in: Proceedings of the 9th Australia New Zealand Conference on Geomechanics, Auckland, p. 7, 2004.

Hyndman, R. D., Currie, C. A., Mazzotti, S., and Frederiksen, A.: Temperature control of continental lithosphere elastic thickness, Te vs Vs, Earth and Planetary Science Letters, 277, 539–548, https://doi.org/10.1016/j.epsl.2008.11.023, 2009.

Iaffaldano, G.: The strength of large-scale plate boundaries: Constraints from the dynamics of the Philippine Sea plate since ~5Ma, Earth and Planetary Science Letters, 357-358, 21–30, https://doi.org/10.1016/j.epsl.2012.09.018, 2012.

Isaacs, A. J., Evans, J. P., Kolesar, P. T., and Nohara, T.: Composition, microstructures, and petrophysics of the Mozumi fault, Japan: In situ analyses of fault zone properties and structure in sedimentary rocks from shallow crustal levels, Journal of Geophysical Research, 113, B12 408, https://doi.org/10.1029/2007JB005314, 2008.

Jaeger, J. C., Cook, N., and Zimmerman, R.: Fundamentals of rock mechanics, Blackwell, Hoboken, New Jersey, 4th edn., 2011.

Konstantinovskaia, E., Malo, M., and Castillo, D. A.: Present-day stress analysis of the St. Lawrence Lowlands sedimentary basin (Canada) and implications for caprock integrity during CO2 injection operations, Tectonophysics, 518-521, 119–137, https://doi.org/10.1016/j.tecto.2011.11.022, 2012.

Krietsch, H., Gischig, V., Evans, K., Doetsch, J., Dutler, N. O., Valley, B., and Amann, F.: Stress Measurements for an In Situ Stimulation Experiment in Crystalline Rock: Integration of Induced Seismicity, Stress Relief and Hydraulic Methods, Rock Mechanics and Rock Engineering, 52, 517–542, https://doi.org/10.1007/s00603-018-1597-8, 2019.

Kruszewski, M., Klee, G., Niederhuber, T., and Heidbach, O.: In situ stress database of the greater Ruhr region (Germany) derived from hydrofracturing tests and borehole logs, Earth System Science Data, 14, 5367–5385, https://doi.org/10.5194/essd-14-5367-2022, 2022.

Li, P., Cai, M., Gorjian, M., Ren, F., Xi, X., and Wang, P.: Interaction between in situ stress states and tectonic faults: A comment, https://doi.org/10.1007/s12613-023-2607-8, 2023.

Lin, W., Yeh, E. C., Hung, J.-H., Haimson, B. C., and Hirono, T.: Localized rotation of principal stress around faults and fractures determined from borehole breakouts in hole B of the Taiwan Chelungpu-fault Drilling Project (TCDP), Tectonophysics, 482, 82–91, https://doi.org/10.1016/j.tecto.2009.06.020, 2010.

Lin, W., Conin, M., Moore, J. C., Chester, F. M., Nakamura, Y., Mori, J. J., Anderson, L., Brodsky, E. E., Eguchi, N., Cook, B., Jeppson, T., Wolfson-Schwehr, M., Sanada, Y., Saito, S., Kido, Y., Hirose, T., Behrmann, J. H., Ikari, M., Ujiie, K., Rowe, C., Kirkpatrick, J., Bose, S., Regalla, C., Remitti, F., Toy, V., Fulton, P., Mishima, T., Yang, T., Sun, T., Ishikawa, T., Sample, J., Takai, K., Kameda, J., Toczko, S., Maeda, L., Kodaira, S., Hino, R., and Saffer, D.: Stress state in the largest displacement area of the 2011 Tohoku-Oki earthquake, Science, 339, 687–690, https://doi.org/10.1126/science.1229379, 2013.

Lockner, D. A., Morrow, C., Moore, D., and Hickman, S. H.: Low strength of deep San Andreas fault gouge from SAFOD core., Nature, 472, 82–85, https://doi.org/10.1038/nature09927, 2011.

Lund Snee, J.-E. and Zoback, M. D.: State of stress in the Permian Basin, Texas and New Mexico: Implications for induced seismicity, Leading Edge, 37, 127–134, https://doi.org/10.1190/tle37020127.1, 2018.

570   Lund Snee, J.-E. and Zoback, M. D.: Multiscale variations of the crustal stress field throughout North America, Nature Communications, 11, 1951, https://doi.org/10.1038/s41467-020-15841-5, 2020.

Maerten, L., Maerten, F., Lejri, M., and Gillespie, P.: Geomechanical paleostress inversion using fracture data, Journal of Structural Geology, 89, 197–213, https://doi.org/10.1016/j.jsg.2016.06.007, 2016.

McLellan, J. G., Oliver, N. H., and Schaubs, P. M.: Fluid flow in extensional environments; numerical modelling with an application to

575   Hamersley iron ores, Journal of Structural Geology, 26, 1157–1171, https://doi.org/10.1016/j.jsg.2003.11.015, 2004.

Meier, S., Bauer, J. F., and Philipp, S. L.: Fault zones in layered carbonate successions: from field data to stress field models, Geomechanics and Geophysics for Geo-Energy and Geo-Resources, 3, 61–93, https://doi.org/10.1007/s40948-016-0047-x, 2017.

Mises, R. v.: Mechanik der festen Körper im plastisch- deformablen Zustand, Nachrichten von der Gesellschaft der Wissenschaften zu Göttingen, Mathematisch-Physikalische Klasse, 1913, 582–592, http://eudml.org/doc/58894, 1913.

580   Moeck, I. and Backers, T.: Fault reactivation potential as a critical factor during reservoir stimulation, First Break, 29, 73–80, https://doi.org/10.3997/1365-2397.2011014, 2011.

Mount, V. S. and Suppe, J.: State of stress near the San Andreas fault: Implications for wrench tectonics, Geology, 15, 1143, https://doi.org/10.1130/0091-7613(1987)15<1143:SOSNTS>2.0.CO;2, 1987.

Mount, V. S. and Suppe, J.: Present-day stress orientations adjacent to active strike-slip faults: California and Sumatra, Journal of Geophysical

585   Research, 97, 11 995, https://doi.org/10.1029/92JB00130, 1992.

Muhuri, S. K., Dewers, T. A., Scott Thurman E., J. E., and Reches, Z.: Interseismic fault strengthening and earthquake-slip instability: Friction or cohesion?, Geology, 31, 881–884, https://doi.org/10.1130/G19601.1, 2003.

Osokina, D.: Hierarchical properties of a stress field and its relation to fault displacements, Journal of Geodynamics, 10, 331–344, https://doi.org/10.1016/0264-3707(88)90039-7, 1988.

590   Pereira, L. C., Guimarães, L. J., Horowitz, B., and Sánchez, M.: Coupled hydro-mechanical fault reactivation analysis incorporating evidence theory for uncertainty quantification, Computers and Geotechnics, 56, 202–215, https://doi.org/10.1016/j.compgeo.2013.12.007, 2014.

Petit, J. P. and Mattauer, M.: Palaeostress superimposition deduced from mesoscale structures in limestone: the Matelles exposure, Languedoc, France, Journal of Structural Geology, 17, 245–256, https://doi.org/10.1016/0191-8141(94)E0039-2, 1995.

Pierdominici, S. and Heidbach, O.: Stress field of Italy - Mean stress orientation at different depths and wave-length of the stress pattern,

595   Tectonophysics, 532-535, 301–311, https://doi.org/10.1016/j.tecto.2012.02.018, 2012.

Pollard, D. D. and Segall, P.: Theoretical Displacements and Stresses Near Fractures in Rock: With Applications To Faults, Joints, Veins, Dikes, and Solution Surfaces, in: Fracture Mechanics of Rock, pp. 277–349, Elsevier, https://doi.org/10.1016/b978-0-12-066266-1.50013-2, 1987.

Prévost, J. H. and Sukumar, N.: Faults simulations for three-dimensional reservoir-geomechanical models with the extended finite element

600   method, Journal of the Mechanics and Physics of Solids, 86, 1–18, https://doi.org/10.1016/j.jmps.2015.09.014, 2016.

Provost, A. S. and Houston, H.: Orientation of the stress field surrounding the creeping section of the San Andreas Fault: Evidence for a narrow mechanically weak fault zone, Journal of Geophysical Research: Solid Earth, 106, 11 373–11 386, https://doi.org/10.1029/2001jb900007, 2001.

Rajabi, M., Tingay, M., Heidbach, O., Hillis, R., and Reynolds, S. D.: The present-day stress field of Australia, Earth-Science Reviews, 168,

605   165–189, https://doi.org/10.1016/j.earscirev.2017.04.003, 2016.

Rajabi, M., Heidbach, O., Tingay, M., and Reiter, K.: Prediction of the present-day stress field in the Australian continental crust using 3D geomechanical–numerical models, Australian Journal of Earth Sciences, 64, 435–454, https://doi.org/10.1080/08120099.2017.1294109, 2017a.

Rajabi, M., Tingay, M., Heidbach, O., Hillis, R., and Reynolds, S.: The present-day stress field of Australia, Earth-Science Reviews, 168, 165–189, https://doi.org/10.1016/j.earscirev.2017.04.003, 2017b.

Rajabi, M., Tingay, M., King, R., and Heidbach, O.: Present-day stress orientation in the Clarence-Moreton Basin of New South Wales, Australia: a new high density dataset reveals local stress rotations, Basin Research, 29, 622–640, https://doi.org/10.1111/bre.12175, 2017c.

Rawnsley, K. D., Rives, T., Petti, J. P., Hencher, S. R., and Lumsden, A. C.: Joint development in perturbed stress fields near faults, Journal of Structural Geology, 14, 939–951, https://doi.org/10.1016/0191-8141(92)90025-R, 1992.

Reiter, K.: Stress rotation – impact and interaction of rock stiffness and faults, Solid Earth, 12, 1287–1307, https://doi.org/10.5194/se-12-1287-2021, 2021.

Reiter, K. and Heidbach, O.: 3-D geomechanical-numerical model of the contemporary crustal stress state in the Alberta Basin (Canada), Solid Earth, 5, 1123–1149, https://doi.org/10.5194/se-5-1123-2014, 2014.

Rispoli, R.: Stress fields about strike-slip faults inferred from stylolites and tension gashes, Tectonophysics, 75, 29–36, https://doi.org/10.1016/0040-1951(81)90274-2, 1981.

Röckel, L., Ahlers, S., Müller, B., Reiter, K., Heidbach, O., Henk, A., Hergert, T., and Schilling, F.: The analysis of slip tendency of major tectonic faults in Germany, Solid Earth, 13, 1087–1105, https://doi.org/10.5194/se-13-1087-2022, 2022.

Sánchez D., M. A., Vásquez, A. R., Van Alstine, D., Butterworth, J., García, J., Carmona, R., Poquioma, W., and Ramones, M.: Applications of Geomechanics in the Development of the Naturally Fractured Carbonates of the Mara Oeste Field, Venezuela, in: Latin American and Caribbean Petroleum Engineering Conference, vol. SPE 54008, p. 8, SPE, Caracas, Venezuela, https://doi.org/10.2118/54008-MS, 1999.

Schellart, W. P.: Shear test results for cohesion and friction coefficients for different granular materials: Scaling implications for their usage in analogue modelling, Tectonophysics, 324, 1–16, https://doi.org/10.1016/S0040-1951(00)00111-6, 2000.

Schoenball, M. and Davatzes, N. C.: Quantifying the heterogeneity of the tectonic stress field using borehole data, Journal of Geophysical Research: Solid Earth, 122, 6737–6756, https://doi.org/10.1002/2017JB014370, 2017.

Schoenball, M., Walsh, F. R., Weingarten, M., and Ellsworth, W. L.: How faults wake up: The Guthrie-Langston, Oklahoma earthquakes, Leading Edge, 37, 100–106, https://doi.org/10.1190/tle37020100.1, 2018.

Schuite, J., Longuevergne, L., Bour, O., Burbey, T. J., Boudin, F., Lavenant, N., and Davy, P.: Understanding the Hydromechanical Behavior of a Fault Zone From Transient Surface Tilt and Fluid Pressure Observations at Hourly Time Scales, Water Resources Research, 53, 10 558–10 582, https://doi.org/10.1002/2017WR020588, 2017.

Segall, P. and Pollard, D. D.: Mechanics of discontinuous faults, Journal of Geophysical Research: Solid Earth, 85, 4337–4350, https://doi.org/10.1029/jb085ib08p04337, 1980.

Seithel, R., Gaucher, E., Müller, B., Steiner, U., and Kohl, T.: Probability of fault reactivation in the Bavarian Molasse Basin, Geothermics, 82, 81–90, https://doi.org/10.1016/j.geothermics.2019.06.004, 2019.

Shi, H., Huang, F., Ma, Z., Wang, Y., Feng, J., and Gao, X.: Mechanical Mechanism of Fault Dislocation Based on in situ Stress State, Frontiers in Earth Science, 8, 1–9, https://doi.org/10.3389/feart.2020.00052, 2020.

Smart, K. J., Ofoegbu, G. I., Morris, A. P., McGinnis, R. N., and Ferrill, D. A.: Geomechanical modeling of hydraulic fracturing: Why mechanical stratigraphy, stress state, and pre-existing structure matter, AAPG Bulletin, 98, 2237–2261, https://doi.org/10.1306/07071413118, 2014.

Sonder, L. J.: Effects of density contrasts on the orientation of stresses in the lithosphere: Relation to principal stress directions in the Transverse Ranges, California, Tectonics, 9, 761–771, https://doi.org/10.1029/TC009i004p00761, 1990.

Stephansson, O. and Ångman, P.: Hydraulic Fracturing Stress Measurements At Forsmark and Stidsvig, Sweden., Bulletin of the Geological Society of Finland, pp. 307–333, https://doi.org/10.17741/bgsf/58.1.021, 1986.

Su, S. and Stephansson, O.: Effect of a fault on in situ stresses studied by the distinct element method, International Journal of Rock Mechanics and Mining Sciences, 36, 1051–1056, https://doi.org/10.1016/S1365-1609(99)00119-7, 1999.

Tamagawa, T. and Pollard, D. D.: Fracture permeability created by perturbed stress fields around active faults in a fractured basement reservoir, AAPG Bulletin, 92, 743–764, https://doi.org/10.1306/02050807013, 2008.

Tenthorey, E. and Cox, S. F.: Cohesive strengthening of fault zones during the interseismic period: An experimental study, Journal of Geophysical Research: Solid Earth, 111, 1–14, https://doi.org/10.1029/2005JB004122, 2006.

Tesauro, M., Kaban, M. K., and Cloetingh, S.: Global strength and elastic thickness of the lithosphere, Global and Planetary Change, 90-91, 51–57, https://doi.org/10.1016/j.gloplacha.2011.12.003, 2012.

Tingay, M. R., Müller, B., Reinecker, J., and Heidbach, O.: State and origin of the present-day stress field in sedimentary basins: New results from the world stress map project, in: Proceedings of the 41st U.S. Rock Mechanics Symposium - ARMA's Golden Rocks 2006 - 50 Years of Rock Mechanics, 41, p. 14, American Rock Mechanics Association, Golden, Colorado, https://www.onepetro.org/conference-paper/ARMA-06-1049, 2006.

Tommasi, A., Vauchez, A., and Daudré, B.: Initiation and propagation of shear zones in a heterogeneous continental lithosphere, Journal of Geophysical Research: Solid Earth, 100, 22 083–22 101, https://doi.org/10.1029/95JB02042, 1995.

Treffeisen, T. and Henk, A.: Elastic and frictional properties of fault zones in reservoir-scale hydro-mechanical models-a sensitivity study, Energies, 13, 25–27, https://doi.org/10.3390/en13184606, 2020a.

Treffeisen, T. and Henk, A.: Representation of faults in reservoir-scale geomechanical finite element models – A comparison of different modelling approaches, Journal of Structural Geology, 131, 103 931, https://doi.org/10.1016/j.jsg.2019.103931, 2020b.

van den Ende, M. P. A. and Niemeijer, A. R.: An investigation into the role of time-dependent cohesion in interseismic fault restrengthening, Scientific Reports, 9, 1–11, https://doi.org/10.1038/s41598-019-46241-5, 2019.

Wang, C., Song, C., Guo, Q., Mao, J., and Zhang, Y.: New insights into stress changes before and after the Wenchuan Earthquake using hydraulic fracturing measurements, Engineering Geology, 194, 98–113, https://doi.org/10.1016/j.enggeo.2015.05.016, 2015.

Xing, H. L., Makinouchi, A., and Mora, P.: Finite element modeling of interacting fault systems, Physics of the Earth and Planetary Interiors, 163, 106–121, https://doi.org/10.1016/j.pepi.2007.05.006, 2007.

Yale, D. P.: Fault and stress magnitude controls on variations in the orientation of in situ stress, Geological Society Special Publication, 209, 55–64, https://doi.org/10.1144/GSL.SP.2003.209.01.06, 2003.

Yoon, J. S., Zang, A., and Stephansson, O.: Numerical investigation on optimized stimulation of intact and naturally fractured deep geothermal reservoirs using hydro-mechanical coupled discrete particles joints model, Geothermics, 52, 165–184, https://doi.org/10.1016/j.geothermics.2014.01.009, 2014.

Yoon, J. S., Stephansson, O., Zang, A., Min, K. B., and Lanaro, F.: Discrete bonded particle modelling of fault activation near a nuclear waste repository site and comparison to static rupture earthquake scaling laws, International Journal of Rock Mechanics and Mining Sciences, 98, 1–9, https://doi.org/10.1016/j.ijrmms.2017.07.008, 2017.

Zhang, S. and Ma, X.: How Does In Situ Stress Rotate Within a Fault Zone? Insights From Explicit Modeling of the Frictional, Fractured Rock Mass, Journal of Geophysical Research: Solid Earth, 126, 1–23, https://doi.org/10.1029/2021JB022348, 2021.

Zhang, Y., Clennell, M. B., Delle Piane, C., Ahmed, S., and Sarout, J.: Numerical modelling of fault reactivation in carbonate rocks under fluid depletion conditions – 2D generic models with a small isolated fault, Journal of Structural Geology, 93, 17–28, https://doi.org/10.1016/j.jsg.2016.10.002, 2016.

685 Zhou, C., Yin, J., Luo, J., and Xiao, G.: Law of geo-stress distribution in the vicinity of fault zone, Journal of Yangtze River Scientific Research Institute, 29, 57–61, https://doi.org/10.3969/j.issn.1001-5485.2012.07.013, 2012.

Zoback, M., Hickman, S., and Ellsworth, W.: Scientific drilling into the San Andreas fault zone - An overview of SAFOD's first five years, Scientific Drilling, pp. 14–28, https://doi.org/10.2204/iodp.sd.11.02.2011, 2011.

Zoback, M. D.: Reservoir Geomechanics, Cambridge University Press, https://doi.org/10.1017/CBO9780511586477, 2010.

690 Zoback, M. D., Zoback, M.-L., Mount, V. S., Suppe, J., Eaton, J. P., Healy, J. H., Oppenheimer, D., Reasenberg, P., Jones, L., Raleigh, C. B., Wong, I. G., Scotti, O., and Wentworth, C.: New Evidence on the State of Stress of the San Andreas Fault System, Science, 238, 1105–1111, https://doi.org/10.1126/science.238.4830.1105, 1987.